ATLAS NOTE

ATLAS-CONF-2012-091

July 6, 2012

Observation of an excess of events in the search for the Standard Model Higgs boson in the $\gamma\gamma$ channel with the ATLAS detector

The ATLAS Collaboration

Abstract

This note reports on a search for the Standard Model Higgs boson in the diphoton decay channel in proton-proton collisions at center-of-mass energies of $\sqrt{s} = 7$ TeV and $\sqrt{s} = 8$ TeV using integrated luminosities of $4.8\,\mathrm{fb}^{-1}$ and $5.9\,\mathrm{fb}^{-1}$, respectively, recorded with the ATLAS detector at the Large Hadron Collider. The search is performed for Higgs boson masses between 110 and 150 GeV.

The expected exclusion limit at 95% confidence level varies between 0.8 and 1.6 times the Standard Model cross section over the studied mass range, and results in an expected exclusion range from 110 GeV to 139.5 GeV. The observed exclusion ranges for a Standard Model Higgs boson are found to be (112 – 122.5) GeV and (132 – 143) GeV at 95% confidence level.

In between the two excluded regions, an excess of events is observed around the diphoton system invariant mass of about 126.5 GeV with a local significance of 4.5σ.

1 Introduction

The search for the Higgs boson [1–3], which is closely tied to the mechanism of electroweak symmetry breaking in the Standard Model (SM), as well as in many models beyond the SM, is one of the key missions of the Large Hadron Collider (LHC) at CERN. The LEP experiments have excluded the existence of a SM Higgs boson with a mass smaller than 114.4 GeV at 95% confidence level [4]. Recent results of the experiments operated at the Tevatron collider exclude at 95% confidence level a SM Higgs boson in the range from 100 GeV to 106 GeV and from 147 GeV to 179 GeV at 95% confidence level [5]. Searches by the ATLAS experiment have narrowed the allowed range for a SM Higgs boson to be between 117.5 GeV and 118.5 GeV, between 122.5 GeV and 129 GeV and above 539 GeV [6], and from the CMS experiment the allowed range is below 127.5 GeV and above 600 GeV [7], where the excluded regions are excluded at 95% confidence level. The search for the Higgs boson decay to two photons strongly contributes to the Higgs boson search in the low mass range, $m_H < 150$ GeV [8, 9]. In the data sample acquired during 2011, ATLAS finds a deviation from the background-only hypothesis at an invariant diphoton mass of 126.5 GeV which corresponds to a local significance of 2.8σ, while the largest deviation reported by CMS corresponds to 3.1σ local significance at a diphoton invariant mass of 124 GeV.

This note presents the analysis strategy and the results of the search for the SM Higgs boson in the diphoton decay channel with the full data sample acquired in 2011, corresponding to $4.8\,\text{fb}^{-1}$ at $\sqrt{s} = 7$ TeV, and the first $5.9\,\text{fb}^{-1}$ of integrated luminosity recorded in 2012 at $\sqrt{s} = 8$ TeV, with the ATLAS detector at the LHC at CERN. The analysis largely follows the previous analysis of the $\sqrt{s} = 7$ TeV data [8], but with substantial improvements. The event categorization has been re-optimized by introducing a category enriched in vector-boson fusion production candidates, which requires an improved selection of the primary vertex associated to the hard interaction. The parametrization of the shape of background distributions has been reconsidered in order to further limit potential biases. A new photon isolation variable has also been adopted, which is less affected by multiple collisions occurring in the same or neighboring bunch crossings, a phenomenon known as "pileup". In addition, a neural-network based photon identification is used for the $\sqrt{s} = 7$ TeV data. For the $\sqrt{s} = 8$ TeV data, a converted photon reconstruction and cut-based photon identification have been introduced which are less sensitive to pileup. Due to the different center-of-mass energies during 2011 and 2012, the two data samples are analyzed separately, and the results are combined statistically.

The note is organized as follows. Sec. 2 introduces the ATLAS detector. Sec. 3 describes the photon reconstruction and the event selection. The categorization of events is detailed in Sec. 4. Sec. 5 contains a discussion of the background modeling, as well as the breakdown of the selected sample into its different components. Sec. 6 summarizes the modeling of the signal decays. Finally, Sec. 7 presents the results of the search.

2 The ATLAS detector and data sample

The ATLAS detector [10] consists of an inner tracking detector surrounded by a superconducting solenoid providing a 2 T magnetic field, electromagnetic and hadron calorimeters, and a muon spectrometer. The main sub-detectors relevant to the search presented here are the calorimeters, in particular the electromagnetic section, and the inner tracking system. The inner detector provides tracking in the pseudorapidity[1] region $|\eta| < 2.5$ and consists of silicon pixel- and microstrip-detectors inside a transition radiation

---

[1] ATLAS uses a right-handed coordinate system with its origin at the nominal interaction point (IP) in the center of the detector and the z-axis along the beam line. the x-axis points from the IP to the center of the LHC ring, and the y-axis points upwards. Cylindrical coordinates (r, ϕ) are used in the transverse plane, ϕ being the azimuthal angle around the beam line. The pseudorapidity is defined in terms of the polar angle θ as $\eta = -\ln\tan\frac{\theta}{2}$. Transverse momentum and energy are defined as $p_T = p\sin\theta$ and $E_T = E\sin\theta$, respectively.

tracker. The tracking detectors consist of a barrel part and two end-cap sections. The transition radiation tracker provides electron identification through transition radiation in scintillating foils and fibers. The electromagnetic calorimeter, a lead/liquid-argon sampling device, is divided in one barrel ($|\eta| < 1.475$) and two end-cap ($1.375 < |\eta| < 3.2$) sections. Longitudinally, it is divided into three layers. The first layer, referred to as the strip layer, has a fine segmentation in η to facilitate the separation of photons from neutral hadrons and to allow the measurement of the shower direction. Most of the energy is deposited in the second layer, and the third layer serves for the correction of the energy deposited downstream of the electromagnetic calorimeter. In the range of $|\eta| < 1.8$ a presampler layer inside the cryostat allows for the correction of energy losses upstream of the calorimeter. The barrel ($|\eta| < 0.8$) and extended barrel ($0.8 < |\eta| < 1.7$) hadron calorimeter sections consist of steel and scintillating tiles, while the end-cap sections ($1.5 < |\eta| < 3.2$) are composed of copper and liquid argon. The forward calorimeter ($3.1 < |\eta| < 4.9$) uses copper and tungsten as absorber with liquid argon as active material.

After the application of data-quality requirements, the data samples amount to 4.8 fb^{-1} at $\sqrt{s} = 7$ TeV and 5.9 fb^{-1} at $\sqrt{s} = 8$ TeV, respectively. The data were recorded with instantaneous luminosity varying between $1 \times 10^{32}\mathrm{cm}^{-2}\mathrm{s}^{-1}$ and $6.8 \times 10^{33}\mathrm{cm}^{-2}\mathrm{s}^{-1}$. The mean number of interactions per bunch crossing has a mean of 9.1 in the data sample acquired during 2011, and of 19.5 for the data taken up to June 2012. The simulation is corrected to reflect the distribution of interactions per bunch crossing and the spread of the z position of the primary vertex observed in data.

The data sample considered in this analysis was selected using a diphoton trigger. In the last step of the triggering chain, two clusters formed from energy depositions in the electromagnetic calorimeter are required. A transverse energy threshold of 20 GeV is required on both clusters for the $\sqrt{s} = 7$ TeV run, while for the $\sqrt{s} = 8$ TeV data sample, the thresholds are increased to 35 GeV and 25 GeV on the leading (most energetic) and subleading (next most energetic) clusters, respectively. In addition, loose criteria are applied on the shapes of the electromagnetic clusters to require them to match the expectations for electromagnetic showers initiated by photons. The trigger has an efficiency greater than 99% for events passing the final event selection.

3 Photon reconstruction and selection of $H \to \gamma\gamma$ candidates

3.1 Photon reconstruction and identification

The photon reconstruction is seeded from clusters of energy deposits in the electromagnetic calorimeter. The reconstruction is designed to separate electrons, unconverted photons, and converted photons, which arise from conversions of photons in the detector material to electron-positron pairs. The clusters are matched to tracks and to conversion vertex candidates, which have been reconstructed in the inner detector and extrapolated to the second layer of the calorimeter [11]. Clusters without any matching track or conversion vertex are classified as unconverted photon candidates. Clusters with a matching vertex reconstructed from one or two tracks are converted photon candidates. For the reconstruction of the $\sqrt{s} = 8$ TeV data, the tracking, vertexing and the matching to clusters have been improved to ensure that the reconstruction of converted photons is robust against pileup. The efficiency of the new photon reconstruction is about 96.5% averaged over the transverse momentum p_{T} and η spectra expected for photons from a Higgs boson decay.

The energies of the clusters are calibrated, separately for unconverted and converted candidates, to account for energy losses upstream of the calorimeter and for energy leakage outside of the cluster. The calibration is refined by applying η-dependent correction factors, which are of the order of $\pm 1\%$, determined from $Z \to e^+e^-$ events. In addition, the energy measurement of converted photons is improved with corrections based on dedicated Monte Carlo simulation (MC) studies. The simulation is corrected to reflect the energy resolution observed using $Z \to e^+e^-$ events in data, which requires an energy smearing of about 1% in the calorimeter barrel region and between 1.2% and up to 2.1% in the calorimeter end-caps. From these studies, the uncertainty on the constant term of the energy resolution is about 50%, while the uncertainty on the energy resolution ranges between 5% and 20% for electrons with $p_{\mathrm{T}} \sim 60$ GeV, depending on the region of the calorimeter [12].

The identification of photons is based on shower shapes measured in the electromagnetic calorimeter. An initial loose cut-based selection, used also at trigger level, is based on shower shapes in the second layer of the electromagnetic calorimeter, as well as the energy deposition in the hadronic calorimeter. A tight identification adds information from the finely segmented strip layer of the calorimeter, which provides good rejection of hadronic jets where a neutral meson carries most of the jet energy. The shower shape values in the simulation are shifted slightly to improve the agreement with the data shower shapes. Two variants of the tight photon identification are used. For the $\sqrt{s} = 7$ TeV data, a neural-network based selection, tuned to achieve similar jet rejection as the cut-based menu used in [8] but with higher efficiency, is used. For the $\sqrt{s} = 8$ TeV data, due to the necessity of ensuring a reliable photon performance for data recorded very recently, a cut-based selection is used, which has been tuned for robustness against pileup effects by relaxing requirements on shower shapes more susceptible to pileup, and tightening others. The photon identification efficiencies, averaged over η, range between 85% and above 95% for the p_{T} range considered for a Higgs boson with mass as low as $m_H = 120$ GeV.

To further suppress hadronic background, an isolation requirement is applied. The isolation transverse energy is estimated by summing the transverse energy of positive-energy topological clusters[2] reconstructed in the electromagnetic and hadronic calorimeters in a cone of $\Delta R = 0.4$ around the photon candidate, where the region within 0.125×0.175 in $\eta \times \phi$ around the photon barycenter is excluded. The isolation is corrected for leakage of the photon energy outside of the excluded region. The positive-energy topological clusters are also used as an input to a low-p_{T} jet algorithm using k_{T} clustering [14,15]. From low-p_{T} jets, the ambient energy in the event from pileup as well as the underlying event is calculated and used to correct the photon isolation event-by-event (for more details see [16] and references therein).

The distribution of the isolation variable has been studied in data and simulation using electrons from $Z \to e^+e^-$ events, and photons from $Z \to e^+e^-\gamma$ events. The data and simulation have been found to be in good agreement and the remaining small discrepancy is accounted for as a systematic uncertainty. In the following, photon candidates are required to have an isolation transverse energy of less than 4 GeV.

3.2 Event and candidate selection

Events are selected by the diphoton trigger and are required to contain at least two reconstructed photon candidates in the fiducial region of the calorimeter, $|\eta| < 1.37$ or $1.52 < |\eta| < 2.37$. The barrel-endcap transition regions, $1.37 < |\eta| < 1.52$ are excluded. To ensure well-reconstructed photon candidates, further quality requirements are applied to the reconstructed clusters. Similarly, converted photon candidates reconstructed from tracks passing through dead modules of the innermost pixel layer are rejected, strongly decreasing the misidentification of electrons as converted photons. Further criteria are applied to the two highest-p_{T} photon candidates. The leading photon candidate is required to have $p_{\mathrm{T}} > 40$ GeV, and the subleading photon candidate $p_{\mathrm{T}} > 30$ GeV. Tight identification criteria as detailed in Sec. 3.1 are applied to both photon candidates. Furthermore, both photon candidates are required to be isolated in the calorimeter.

With this selection, 23788 diphoton candidates are observed in the diphoton invariant mass range between 100 and 160 GeV in the $\sqrt{s} = 7$ TeV data sample. In the same mass range, 35271 events are selected in the $\sqrt{s} = 8$ TeV data sample.

---

[2] Topological clusters are three-dimensional clusters of variable size, built by associating calorimeter cells on the basis of the signal-to-noise ratio [13].

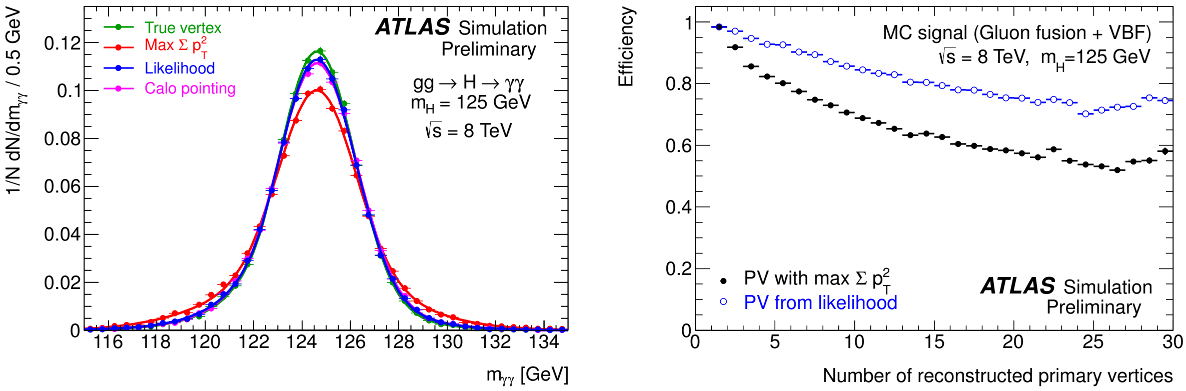

Figure 1: Left: distribution of the expected diphoton mass for $H \to \gamma\gamma$ signal events as a function of the algorithm used to determine the longitudinal vertex position of the hard-scattering event. The use of the calorimeter information, labelled as ”Calo pointing” is fully adequate to reach the optimal achievable mass resolution labelled as ”True vertex”. The likelihood described in the text, combining this information with the primary vertex information from the tracking, provides similar mass resolution. Right: the dependence of the efficiency for selecting a reconstructed primary vertex within $\Delta z = 0.2$ mm of the true hard interaction vertex using two different methods: the highest $\sum p_{\mathrm{T}}^2$ of all tracks assigned to a vertex (black) and from the likelihood as described in the text (blue). The addition of the tracking information from the inner detector is necessary to improve the efficiency of identification of the hard-interaction primary vertex needed for the jet selection.

3.3 Trigger efficiency

The efficiency of the trigger for events passing the analysis selection is determined by a bootstrap approach: the efficiency of the trigger selection with respect to offline photons is factorized as the high-level trigger selection efficiency relative to the Level-1 seed, multiplied by the Level-1 seed efficiency. These efficiencies are evaluated from unbiased events, as described in [17].

The efficiency of the diphoton trigger used for the $\sqrt{s} = 7$ TeV data is measured to be $(98.9 \pm 0.2)\%$. The efficiency of the diphoton trigger for the $\sqrt{s} = 8$ TeV data is found to be $(99.6 \pm 0.1)\%$. No dependence on pileup is observed on $\sqrt{s} = 8$ TeV data for loose photon triggers up to 25 primary vertices per event. To estimate the systematic uncertainty due to the method and to the unknown composition of the data sample, the efficiency of the loose diphoton trigger was also evaluated using a tag and probe method on $Z \to e^+e^-\gamma$ data events when one of the electrons radiates a photon, using a simulated $H \to \gamma\gamma$ sample and from simulated events containing jets misidentified as photons. The difference with respect to the efficiency computed with the bootstrap approach results in a systematic uncertainty of less than 1%.

3.4 Primary vertex selection and estimation of the diphoton invariant mass

The selection of the primary vertex is relevant for two aspects of the analysis: the estimation of the invariant mass of the diphoton system, and the selection of the jets associated with the hard interaction, as described in Sec. 4. While the former only has requirements on the resolution of the primary vertex position, the latter requires the identification of a specific vertex.

The primary vertex of the hard interaction is identified by combining the following elements in a global likelihood: the directions of flight of the photons as determined by the measurements using the longitudinal segmentation of the calorimeter, the average beam spot position, and the $\sum p_{\mathrm{T}}^2$ of the tracks associated with each reconstructed vertex. In case of the $\sqrt{s} = 7$ TeV data, the conversion vertex is also used in the likelihood for converted photons with tracks containing silicon hits. As shown in Fig. 1 (left), the calorimeter information (with a resolution of $\sigma_z \sim 15\,\mathrm{mm}$ using only the calorimeter pointing, and $\sigma_z \sim 6\,\mathrm{mm}$ for two converted photons with silicon hits, if the vertex information is used) is sufficient to improve the mass resolution and is very close to the optimal resolution that can be achieved by using the true hard scattering primary vertex position. The mass resolution is similar when the likelihood is used to select the primary vertex. The addition of the tracking information from the inner detector is necessary to improve the identification of the hard-interaction primary vertex needed for the jet selection. Fig. 1 (left) shows the efficiency of finding the correct primary vertex as a function of the number of reconstructed vertices in the event using different methods. The decrease of the efficiency of finding the correct hard interaction primary vertex at high pileup can lead to an inefficiency in identifying the jets that accompany the Higgs boson production.

The invariant mass of the two photons is then estimated using the photon energies as measured in the calorimeter, ϕ as determined from the position of the photon in the calorimeter, and η as determined by the identified primary vertex and the photon impact point in the calorimeter.

4 Jet reconstruction and event categorization

Classifying events into subsamples with different signal-to-background ratios and different invariant mass resolutions improves the sensitivity of the search [18]. Multiple event properties are used for the categorization:

- the η region of the two photons in the calorimeter,
- whether the photon candidates are converted or unconverted,
- the p_{Tt} [19,20] of the diphoton system. The p_{Tt} of the diphoton system is defined as the orthogonal component of the diphoton momentum when projected on the axis $\hat{t}$ given by the difference of the photon momenta $\vec{p}_{\mathrm{T}}^{\,\gamma 1}$ and $\vec{p}_{\mathrm{T}}^{\,\gamma 2}$. Thus, $p_{\mathrm{Tt}} = |(\vec{p}_{\mathrm{T}}^{\,\gamma 1} + \vec{p}_{\mathrm{T}}^{\,\gamma 2}) \times \hat{t}|$, where $\hat{t} = (\vec{p}_{\mathrm{T}}^{\,\gamma 1} - \vec{p}_{\mathrm{T}}^{\,\gamma 2})/|\vec{p}_{\mathrm{T}}^{\,\gamma 1} - \vec{p}_{\mathrm{T}}^{\,\gamma 2}|$. Events with $p_{\mathrm{Tt}} < 60$ GeV form the low-p_{Tt} sample, while the remaining events form the high-p_{Tt} sample.
- whether an event passes the 2-jets selection with a vector-boson fusion-like signature, described in Sec. 4.1.

The variable p_{Tt} is strongly correlated with the diphoton transverse momentum, but it has a better detector resolution and retains a monotonically falling diphoton invariant mass distribution for the background events in the search region given the chosen cut values (see below). The latter quality is advantageous for the background modeling and associated uncertainties discussed below. The p_{Tt} distribution in simulated background events and in simulated Higgs boson events is shown in Fig. 2 normalized to the same area. The background is obtained from SM $\gamma\gamma$ MC simulated with SHERPA [21] and γ-jet MC simulated with ALPGEN [22]. The two contributions have been normalized to their respective fractions observed on data (see Sec. 5), while the small jet-jet and Drell-Yan components have been neglected. Fig. 2 also shows the difference in the p_{Tt} distribution for different Higgs boson production processes, which can serve for their separation in addition to jet-based selections.

4.1 2-Jets selection

The dominant SM Higgs boson production process is gluon fusion. The second-most prominent production process is vector-boson fusion (VBF). The VBF signature consists of two forward jets, with little

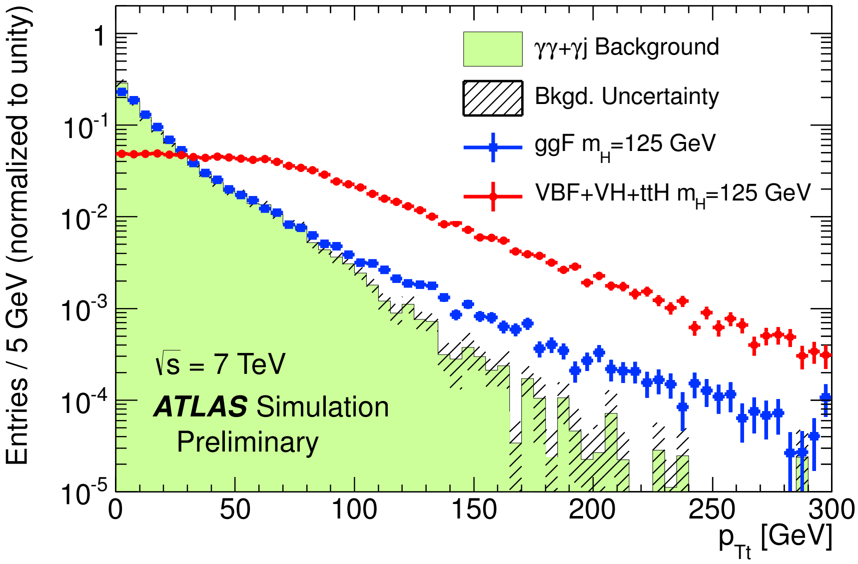

Figure 2: Distribution of p_{Tt} in simulated events with Higgs boson production and in background events. The signal distribution is shown separately for gluon fusion (blue), and vector-boson fusion together with associated production (red). The background MC samples are described in the text. The background MC and the two signal distributions are normalized to unit area.

QCD radiation in the central region from the hard interaction.

Jets are reconstructed using the anti-k_{t} algorithm [23] with distance parameter $R = 0.4$. The inputs to the jet finding are three-dimensional topological calorimeter clusters [13, 24, 25] taken at the electromagnetic (EM) scale. The jets are calibrated in three steps. First, the dependence of the jet response to the number of primary vertices and the average number of interactions is removed by applying a pileup correction derived from simulated samples [26]. Second, a jet origin correction [25] that adjusts the direction of the jet such that it points back to the primary vertex identified as the one with the highest $\sum p_{\mathrm{T}}^2$ of the associated tracks is applied. Finally, a MC-derived energy and pseudorapidity dependent correction [25] is applied. For the $\sqrt{s} = 7$ TeV data, residual data-driven calibrations are derived using various in situ techniques that exploit the transverse momentum balance between a jet and a reference object, and are applied to the jet four-momenta [27].

A subsample of the data is enriched in VBF events by applying the following 2-jets selection:

- The event must have at least two hadronic jets with $\left|\eta^{\mathrm{jet}}\right| < 4.5$ and $p_{\mathrm{T}}^{\mathrm{jet}} > 25$ GeV. For the $\sqrt{s} = 8$ TeV analysis, the $p_{\mathrm{T}}^{\mathrm{jet}}$ cut is raised to 30 GeV for jets with $2.5 < |\eta| < 4.5$. Jets in the tracker acceptance range ($|\eta| < 2.5$) are required to have a jet-vertex-fraction of at least 0.75. The jet-vertex-fraction is defined as the fraction of the sum of p_{T} carried by tracks in the jet and associated to the primary vertex selected with the likelihood method with respect to the total p_T carried by all the tracks associated to the jet. The jets are required to pass jet quality cuts and to have a minimum distance $\Delta R = 0.4$ to any of the selected photons. Among the selected jets, the two jets with the highest p_{T} are considered as the tagging jets.

- The pseudorapidity gap between the tagging jets, $\Delta\eta_{jj}$, has to be larger than 2.8.

- The invariant mass of the tagging jets, m_{jj}, has to be larger than 400 GeV.

- The azimuthal angle difference $\Delta\phi$ between the diphoton system and the system of the two tagging jets has to be larger than 2.6.

For simulated VBF events, the efficiency of the 2-jets selection is 29% for the $\sqrt{s} = 7$ TeV analysis and 24% for the $\sqrt{s} = 8$ TeV analysis.

The fraction of selected diphoton data events that pass the 2-jets selection is found to depend only weakly on the number of reconstructed primary vertices.

4.2 Event categories

As explained above, the event sample is split into exclusive categories. Events passing the 2-jets selection are excluded from the other categories.

1. Unconverted central, low p_{Tt}: Both photon candidates are reconstructed as unconverted photons and have $|\eta| < 0.75$. The diphoton system has low p_{Tt}.
2. Unconverted central, high p_{Tt}: Both photon candidates are reconstructed as unconverted photons and have $|\eta| < 0.75$. The diphoton system has high p_{Tt}.
3. Unconverted rest, low p_{Tt}: Both photon candidates are reconstructed as unconverted photons and at least one candidate has $|\eta| > 0.75$. The diphoton system has low p_{Tt}.
4. Unconverted rest, high p_{Tt}: Both photon candidates are reconstructed as unconverted photons and at least one candidate has $|\eta| > 0.75$. The diphoton system has high p_{Tt}.
5. Converted central, low p_{Tt}: At least one photon candidate is reconstructed as converted photon and both photon candidates have $|\eta| < 0.75$. The diphoton system has low p_{Tt}.
6. Converted central, high p_{Tt}: At least one photon candidate is reconstructed as converted photon and both photon candidates have $|\eta| < 0.75$. The diphoton system has high p_{Tt}.
7. Converted rest, low p_{Tt}: At least one photon candidate is reconstructed as a converted photon and both photon candidates have $|\eta| < 1.3$ or $|\eta| > 1.75$, but at least one photon candidate has $|\eta| > 0.75$. The diphoton system has low p_{Tt}.
8. Converted rest, high p_{Tt}: At least one photon candidate is reconstructed as a converted photon and both photon candidates have $|\eta| < 1.3$ or $|\eta| > 1.75$, but at least one photon candidate has $|\eta| > 0.75$. The diphoton system has high p_{Tt}.
9. Converted transition: At least one photon candidate is reconstructed as a converted photon and at least one photon candidate is in the range $1.3 < |\eta| < 1.37$ or $1.52 < |\eta| < 1.75$.
10. 2-jets: The event passes the 2-jets selection to enrich in VBF final states as described in Sec. 4.1.

The number of events observed in the different categories in the diphoton invariant mass range between 100 and 160 GeV for the analyzed datasets is given in Table 1. In addition, the data sample is studied without categorization. This is referred to as the inclusive sample.

The contribution of each category to the analysis depends on its mass resolution, its signal-to-background ratio and its statistical power. Table 2 shows the expected number of signal and background events at $\sqrt{s} = 8$ TeV and their ratio in a window around $m_H = 126.5$ GeV that would contain 90% of the signal events, along with the observed number of events in this window. The number of background events has been obtained from a fit to the invariant mass distribution as described in Sec. 5. Table 2 is representative of the sensitivity to a Higgs boson signal with a mass in the region of $(120 - 130)$ GeV.

Table 1: Number of events observed in the different categories in 4.8 fb^{-1} of $\sqrt{s}$ = 7 TeV data and 5.9 fb^{-1} of $\sqrt{s}$ = 8 TeV data in the diphoton invariant mass range between 100 GeV and 160 GeV.

Category	$\sqrt{s}$ = 7 TeV data [N_{evt}]	$\sqrt{s}$ = 8 TeV data [N_{evt}]
Unconverted central, low p_{Tt}	2054	2945
Unconverted central, high p_{Tt}	97	173
Unconverted rest, low p_{Tt}	7129	12136
Unconverted rest, high p_{Tt}	444	785
Converted central, low p_{Tt}	1493	2021
Converted central, high p_{Tt}	77	113
Converted rest, low p_{Tt}	8313	11112
Converted rest, high p_{Tt}	501	708
Converted transition	3591	5149
2-jets	89	129
Total	23788	35271

The FWHM and the resolution of the expected signal as discussed in Sec. 6 are also given. The “central” categories, where both photons pass through the region with less material in front of the calorimeter, show the best invariant mass resolution, while it is lower for categories with photons reconstructed in other regions of the calorimeter.

5 Background composition and modeling

5.1 Background composition

The main processes contributing to the background in the $H \to \gamma\gamma$ search can be divided into two classes: the irreducible background consisting of QCD diphoton production, and the reducible background consisting of associated production of a photon with jets and processes with several jets in the final state. The last two contribute to the background when one or two jets fragmenting into neutral mesons (mainly π^0) are misidentified as prompt photons. Understanding the composition of the selected sample serves as a monitoring of the performance of the photon identification, as well as a validation of the description of the backgrounds to the $H \to \gamma\gamma$ search in the simulation. The latter is an important ingredient to the choice of the background parametrization, where also the sample composition determined from data is used.

Several methods based on varying photon identification and isolation criteria are used to determine the composition of the diphoton candidate events [28, 29]. They yield consistent results within their uncertainties. The fraction of diphoton events in the selected sample has been estimated to be $(80 \pm 4)\%$ in the $\sqrt{s}$ = 7 TeV data and $(75^{+3}_{-2})\%$ in the $\sqrt{s}$ = 8 TeV data. The fraction of γ-jet and jet-jet events has been found to be $(19 \pm 3)\%$ $((22 \pm 2)\%)$ and $(1.8 \pm 0.5)\%$ $((2.6 \pm 0.5)\%)$ in the $\sqrt{s}$ = 7(8) TeV data sample. Fig. 3 shows the composition of the diphoton invariant mass spectrum, presented in bins of 1 GeV.

Background from Drell-Yan processes arises through the mis-reconstruction of electrons as photons, mostly through reconstruction of electrons as converted photons. Electrons from Drell-Yan processes have an isolation profile similar to that of signal photons. The misidentification rates are measured by using $Z \to e^+e^-$ data events reconstructed as dielectron and e-γ pairs. For the $\sqrt{s}$ = 7 TeV data, the Drell-Yan background in the mass region (100 − 160) GeV is estimated to be $N^{DY}_{\gamma\gamma} = 325 \pm 3(\mathrm{stat}) \pm 30(\mathrm{syst})$. For the $\sqrt{s}$ = 8 TeV data, the Drell-Yan background in the region (100 − 160) GeV is estimated to be

Table 2: Number of expected signal S and background events B in mass a window around m_H = 126.5 GeV that would contain 90% of the expected signal events, along with the observed number of events in this window. In addition, σ_{CB}, the Gaussian width of the Crystal Ball function describing the invariant mass distribution (see Sec. 6), and the FWHM of the distribution, are given. The numbers are given for the data and simulation at $\sqrt{s}$ = 8 TeV for different categories and the inclusive sample.

Category	σ_{CB} [GeV]	FWHM [GeV]	Observed [N_{evt}]	S [N_{evt}]	B [N_{evt}]
Inclusive	1.63	3.87	3693	100.4	3635
Unconverted central, low p_{Tt}	1.45	3.42	235	13.0	215
Unconverted central, high p_{Tt}	1.37	3.23	15	2.3	14
Unconverted rest, low p_{Tt}	1.57	3.72	1131	28.3	1133
Unconverted rest, high p_{Tt}	1.51	3.55	75	4.8	68
Converted central, low p_{Tt}	1.67	3.94	208	8.2	193
Converted central, high p_{Tt}	1.50	3.54	13	1.5	10
Converted rest, low p_{Tt}	1.93	4.54	1350	24.6	1346
Converted rest, high p_{Tt}	1.68	3.96	69	4.1	72
Converted transition	2.65	6.24	880	11.7	845
2-jets	1.57	3.70	18	2.6	12

$N_{\gamma\gamma}^{DY}$ = 270 ± 4(stat) ± 24(syst). The lower level of Drell-Yan background in the $\sqrt{s}$ = 8 TeV data is due to the improvements in the reconstruction of converted photons. The background from Drell-Yan processes is located in the low invariant mass region as can be seen in Fig. 4 for the $\sqrt{s}$ = 8 TeV sample and is very small in the invariant mass region used in this analysis.

5.2 Background modeling

For statistical analysis of the measured diphoton spectrum, the background is parametrized by an analytic function for each category, where the normalization and the shape are obtained from fits to the diphoton invariant mass distribution. Different parametrizations are chosen for the different event categories to achieve a good compromise between limiting the size of a potential bias introduced by the chosen parametrization and retaining good statistical power. Depending on the category, an exponential function, a fourth-order Bernstein polynomial or an exponential function of a second-order polynomial is used (see Table 3). For the analysis of the inclusive sample, a fourth-order Bernstein polynomial is used.

Potential biases from the choice of background parametrization are estimated using three different sets of high statistics background-only MC models. The prompt diphoton background is obtained from the three generators RESBOS [30], DIPHOX [31], and SHERPA [21], while the same reducible background samples are used for all three models. These are based on SHERPA for the γ-jet background and on PYTHIA6 [32] for the jet-jet background. Detector effects are included in some samples with with weighting and smearing techniques. In the SHERPA and PYTHIA samples, detector effects are taken into account, including photon identification efficiency, photon energy resolution, the process of photons being faked by jets, and the fraction of converted photons in the different detector regions. In the RESBOS and DIPHOX samples, the effect of photon identification efficiency is taken into account. In addition, the Drell-Yan background component is taken into account; the shape and number of events for this background is extracted from data-driven studies (see above). Each of these MC models is mixed

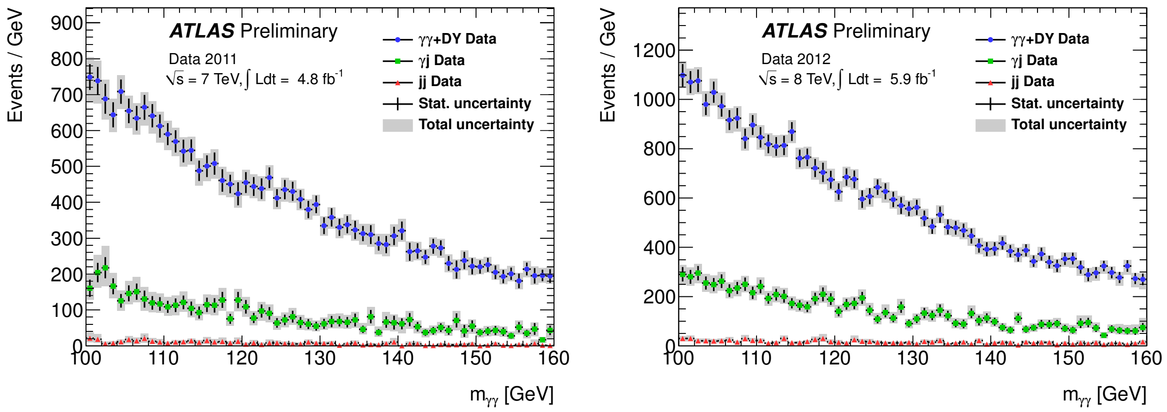

Figure 3: Diphoton sample composition as a function of the invariant mass for the $\sqrt{s}$ = 7 TeV (left) and the $\sqrt{s}$ = 8 TeV (right) dataset. The small contribution from Drell-Yan events is included in the diphoton component.

from the different components in the proportions estimated from data and is normalized to the total number of events observed in the data.

A variety of functional forms are considered for the background parametrization: single and double exponential functions, Bernstein polynomials up to seventh order, exponentials of second and third-order polynomials, and exponentials with modified turn-on behavior. The potential bias for a given parametrization is estimated by performing a maximum likelihood fit in the mass range of (100 – 160) GeV using the sum of a signal and the background parametrization to all three sets of background-only simulation models for each category. The signal shape is taken to follow the expectation for an SM Higgs (see Sec. 6) in terms of shape, with a mass between 110 GeV and 150 GeV, and with the normalization floating. The categories mainly affected by background parametrization bias are the high-statistics categories, which also have a lower signal to background ratio. Parametrizations that exhibit problems with fit convergence are discarded. Parametrizations for which the estimated potential bias is smaller than 20% of the uncertainty on the fitted signal yield, or where the bias is smaller than 10% of the number of expected signal events for each of the background models are selected for further studies. Among these selected parametrizations, the parametrization with the best expected sensitivity at m_H = 125 GeV is selected as the background parametrization. For categories with low statistics, an exponential function is found to have sufficiently small bias, while polynomials and exponentials of polynomials, respectively, are needed for limiting the potential bias to stay within the predefined requirements for the higher-statistics categories.

For the chosen parametrization, the largest observed absolute signal yield over the full mass range studied (from 110 GeV to 150 GeV) is used as the potential bias for a given category, using the background model based on SHERPA for the diphoton component. The selected parametrizations along with their potential bias, which is taken as an estimate of the systematic uncertainty due to the choice of parametrization, are shown in Table 3.

The invariant mass distributions and their composition obtained from the high-statistics simulation model based on SHERPA for the diphoton component have been cross checked against data in different categories, using the same background decomposition method as used for the inclusive sample (see Sec. 5.1). Within the statistical uncertainties of data, a good agreement is found for the shapes of the invariant mass distributions. The invariant mass distributions of the different categories have also been compared with invariant mass distributions in a signal-depleted sample based on reversal of the photon isolation selection. After accounting for the different sample composition in the isolation signal and

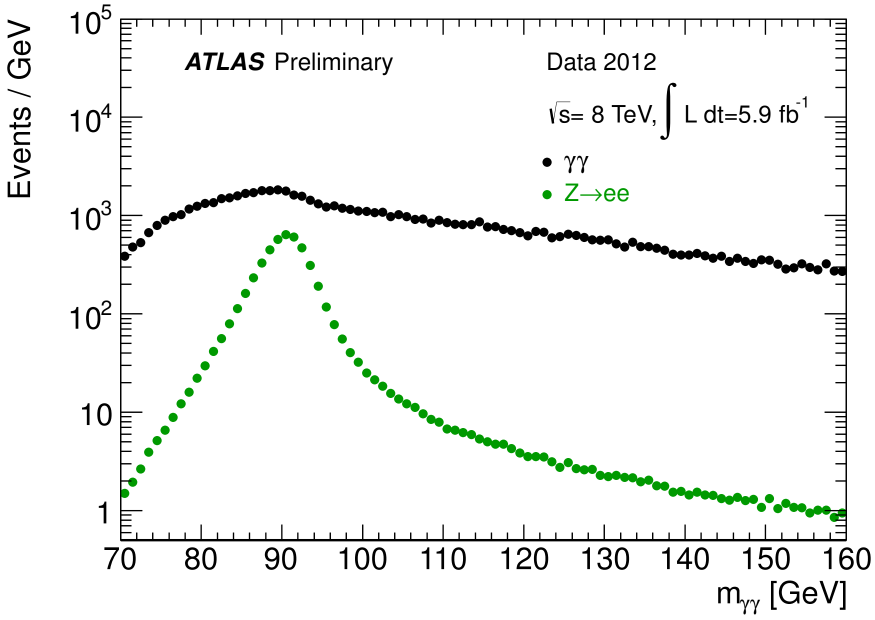

Figure 4: Invariant mass distribution after applying the diphoton selection: Data (black) and estimated contribution of $Z \to e^+e^-$ events to the diphoton invariant mass distribution (green) for the $\sqrt{s}$ = 8 TeV sample. This background contribution is obtained from reconstructed $Z \to e^+e^-$ events in data.

sideband regions, a good agreement of the invariant mass distributions is found.

6 Signal modeling

The modeling of the signal, both in terms of Higgs boson production, and of detector response to a $H \to \gamma\gamma$ signal, is essential to set upper limits on the SM Higgs boson production cross section, and will be equally needed to study the properties of a potential signal. This section shows the modeling of the $H \to \gamma\gamma$ signal and describes the corrections that are applied, as well as the systematic uncertainties that are assigned.

6.1 Signal simulation

Higgs boson production and decay are simulated with several MC samples that are passed through a full detector simulation [33] using GEANT4 [34]. Pileup effects are simulated by overlaying each MC event with a variable number of simulated inelastic proton-proton collisions [35]. POWHEG [36, 37], interfaced to PYTHIA6 [32] for $\sqrt{s}$ = 7 TeV and PYTHIA8 [38] for $\sqrt{s}$ = 8 TeV for showering and hadronization, is used for generation of gluon fusion and VBF production. PYTHIA6 for $\sqrt{s}$ = 7 TeV and PYTHIA8 for $\sqrt{s}$ = 8 TeV are used to generate the Higgs boson production in association with W/Z and $t\bar{t}$.

The Higgs boson production cross sections are computed up to next-to-next-to-leading order (NNLO) [39–44] in QCD for the gluon fusion process. In addition, QCD soft-gluon resummations up to next-to-next-to-leading logarithmic order (NNLL) improve the NNLO calculation [45, 46] and are used through event reweighting for the $\sqrt{s}$ = 7 TeV simulation. For the $\sqrt{s}$ = 8 TeV simulation, a Higgs boson p_{T}

Table 3: Systematic uncertainty on the number of signal events fitted due to the background parametrization, given in number of events. Three different background parametrizations are used depending on the category, an exponential function, a fourth-order Bernstein polynomial and the exponential of a second-order polynomial.

Category	Parametrization	Uncertainty [N_{evt}]	
		$\sqrt{s}$ = 7 TeV	$\sqrt{s}$ = 8 TeV
Inclusive	4th order pol.	7.3	10.6
Unconverted central, low p_{Tt}	Exp. of 2nd order pol.	2.1	3.0
Unconverted central, high p_{Tt}	Exponential	0.2	0.3
Unconverted rest, low p_{Tt}	4th order pol.	2.2	3.3
Unconverted rest, high p_{Tt}	Exponential	0.5	0.8
Converted central, low p_{Tt}	Exp. of 2nd order pol.	1.6	2.3
Converted central, high p_{Tt}	Exponential	0.3	0.4
Converted rest, low p_{Tt}	4th order pol.	4.6	6.8
Converted rest, high p_{Tt}	Exponential	0.5	0.7
Converted transition	Exp. of 2nd order pol.	3.2	4.6
2-jets	Exponential	0.4	0.6

Table 4: Higgs boson production cross section σ (total and the contributions from gluon fusion and VBF) in pb for a SM Higgs boson with m_H = 125 GeV for $\sqrt{s}$ = 7 TeV and $\sqrt{s}$ = 8 TeV [67], as well as the branching ratio $\mathcal{B}$ of Higgs boson decaying to two photons [67].

$\sqrt{s}$	m_H	$\mathcal{B}(H \to \gamma\gamma)$	$\sigma(pp \to H)$	$\sigma(gg \to H)$	σ_{VBF}
7 TeV	125 GeV	2.3×10^{-3}	17.5 pb	15.3 pb	1.2 pb
8 TeV	125 GeV	2.3×10^{-3}	22.3 pb	19.5 pb	1.6 pb

tuning and finite mass effects are taken into account directly in POWHEG [47]. The next-to-leading order (NLO) EW corrections are applied [48,49]. These results are compiled in [50–52] assuming factorization between QCD and EW corrections. The cross sections for the VBF process are calculated with full NLO QCD and EW corrections [53–55], and approximate NNLO QCD corrections are applied [56]. The W/ZH processes are calculated at NLO [57] and at NNLO [58], and NLO EW radiative corrections [59] are applied. The full NLO QCD corrections for $t\bar{t}H$ are calculated [60–63]. The Higgs boson cross sections, branching ratios [64–66] and their uncertainties are compiled in [47,67].

The production cross section for a Higgs boson with m_H = 125 GeV is given in Table 4, which also details the contributions from gluon fusion and vector-boson fusion and the Higgs boson decay branching fraction to two photons. The yields for gluon fusion are, in the following, corrected for destructive interference with the $gg \to \gamma\gamma$ process [68]. These corrections range between −2% and −5%, depending on the diphoton invariant mass.

6.2 Signal efficiency and yield

The expected Higgs boson signal efficiency and yields are computed and summarized in Table 5. The expected signal yield for the different production processes is normalized to an integrated luminosity of 4.8 fb^{-1} for the $\sqrt{s}$ = 7 TeV data and to 5.9 fb^{-1} for the $\sqrt{s}$ = 8 TeV data, along with the selection

Table 5: Expected Higgs boson signal efficiency ϵ (including acceptance of kinematic selections as well as photon identification and isolation efficiencies) and event yield for $H \to \gamma\gamma$ assuming an integrated luminosity of 4.8 fb^{-1} for the $\sqrt{s}$ = 7 TeV data (top) and of 5.9 fb^{-1} for the $\sqrt{s}$ = 8 TeV data (bottom). Results are given for different production processes.

$\sqrt{s}$	m_H [GeV]	$gg \to H$		VBF		WH		ZH		ttH		Total
		ϵ(%)	N_{evt}	ϵ(%)	N_{evt}	ϵ(%)	N_{evt}	ϵ(%)	N_{evt}	ϵ(%)	N_{evt}	N_{evt}
7 TeV	110	37.3	71.7	37.9	5.2	33.5	2.8	33.5	1.5	33.7	0.4	81.6
	115	39.5	73.8	40.1	5.5	34.9	2.8	35.5	1.5	34.9	0.3	83.9
	120	40.9	73.5	42.1	5.8	37.0	2.6	36.9	1.4	35.9	0.3	83.6
	125	42.0	70.9	43.8	5.8	38.1	2.4	38.4	1.3	37.2	0.3	80.7
	130	43.1	66.3	44.8	5.7	39.3	2.1	39.9	1.2	37.8	0.3	75.6
	135	44.6	59.8	46.9	5.3	40.7	1.8	40.8	1.0	38.7	0.2	68.1
	140	45.2	51.7	48.7	4.8	41.8	1.5	42.3	0.9	39.5	0.2	59.1
	145	45.8	42.3	49.8	4.1	42.5	1.2	43.6	0.7	40.5	0.2	48.5
	150	45.8	31.6	49.7	3.1	44.1	0.9	44.7	0.5	40.7	0.1	36.2
8 TeV	110	33.8	100.6	34.5	7.4	29.9	3.7	29.5	2.1	27.3	0.6	114.4
	115	35.6	103.8	36.2	7.9	30.6	3.6	32.5	2.1	27.9	0.6	118.0
	120	37.2	103.6	38.1	8.2	32.7	3.4	32.9	2.0	29.4	0.6	117.8
	125	38.3	100.3	39.6	8.3	33.9	3.2	34.2	1.8	29.7	0.5	114.1
	130	39.1	94.1	41.2	8.0	35.1	2.8	35.9	1.6	31.1	0.5	107.0
	135	40.4	85.3	42.4	7.6	35.7	2.4	36.6	1.4	32.2	0.4	97.1
	140	41.1	74.0	43.0	6.8	37.0	2.0	36.8	1.2	32.4	0.3	84.3
	145	41.6	60.6	43.7	5.8	38.0	1.6	38.5	0.9	33.6	0.3	69.2
	150	41.7	45.3	44.8	4.4	38.2	1.1	39.2	0.7	34.0	0.2	51.7

efficiencies. The last column displays the total expected number of $H \to \gamma\gamma$ signal events after the application of the event selection specified above, depending on the Higgs boson mass. The composition of the different categories is given in Table 6.

6.2.1 Systematic uncertainty on the expected signal yields

In this section a brief description of the systematic uncertainties considered for the calculation of the expected signal yields with MC is given.

- Luminosity. The uncertainty on the integrated luminosity is 1.8% for the $\sqrt{s}$ = 7 TeV data and 3.6% for the $\sqrt{s}$ = 8 TeV data [69].
- Trigger Efficiency. The uncertainty on the trigger efficiency is 1% per event (see Sec.3.3).
- Photon identification. The uncertainty on the photon identification is based on the comparison of the efficiency obtained using MC and various data-driven measurements based on photons from $Z \to e^+e^-\gamma$, electrons from $Z \to e^+e^-$ and a sideband technique. For the neural-network photon identification, a relative systematic uncertainty of 4% is assigned per photon for most η regions (for unconverted photons the uncertainty is 5% for $1.52 < |\eta| < 1.81$ and 7% in $1.81 < |\eta| < 2.37$). Treating the uncertainty as fully correlated between the two photons, this translates to a relative uncertainty on the efficiency per event of 8.4%. For the tight identification used for the analysis of the $\sqrt{s}$ = 8 TeV data, a 5% relative uncertainty is assigned for photons in the barrel region of the calorimeter, $|\eta| < 1.37$, and a 7% uncertainty is assigned for photons in the calorimeter endcap region, $1.52 < |\eta| < 2.37$. Treating the uncertainties as fully correlated between the two photons, this results in a relative event-level uncertainty of 10.8%.

Table 6: Number of expected signal events per category at $m_H = 126.5$ GeV, at $\sqrt{s} = 7$ TeV (top) and $\sqrt{s} = 8$ TeV (bottom) and breakdown by production process.

$\sqrt{s}$	Category	Events	$gg \to H$ [%]	VBF [%]	WH [%]	ZH [%]	ttH [%]
7 TeV	Inclusive	79.3	87.8	7.3	2.9	1.6	0.4
	Unconverted central, low p_{Tt}	10.4	92.9	4.0	1.8	1.0	0.2
	Unconverted central, high p_{Tt}	1.5	66.5	15.7	9.9	5.7	2.4
	Unconverted rest, low p_{Tt}	21.6	92.8	3.9	2	1.1	0.2
	Unconverted rest, high p_{Tt}	2.7	65.4	16.1	10.8	6.1	1.8
	Converted central, low p_{Tt}	6.7	92.8	4.0	1.9	1.0	0.2
	Converted central, high p_{Tt}	1.0	66.6	15.3	10	5.7	2.5
	Converted rest, low p_{Tt}	21.0	92.8	3.8	2.0	1.1	0.2
	Converted rest, high p_{Tt}	2.7	65.3	16.0	11.0	5.9	1.8
	Converted transition	9.5	89.4	5.2	3.3	1.7	0.3
	2-jets	2.2	22.5	76.7	0.4	0.2	0.1
8 TeV	Inclusive	111.6	88.5	7.4	2.7	1.6	0.5
	Unconverted central, low p_{Tt}	14.4	92.9	4.2	1.7	1.0	0.2
	Unconverted central, high p_{Tt}	2.5	72.5	14.1	6.9	4.2	2.3
	Unconverted rest, low p_{Tt}	31.4	92.5	4.1	2.0	1.1	0.2
	Unconverted rest, high p_{Tt}	5.3	72.1	13.8	7.8	4.6	1.7
	Converted central, low p_{Tt}	9.1	92.8	4.3	1.7	1.0	0.3
	Converted central, high p_{Tt}	1.6	72.7	13.7	7.1	4.1	2.3
	Converted rest, low p_{Tt}	27.3	92.5	4.2	2.0	1.1	0.2
	Converted rest, high p_{Tt}	4.6	70.8	14.4	8.3	4.7	1.7
	Converted transition	13.0	88.8	6.0	3.1	1.8	0.4
	2-jets	2.9	30.4	68.4	0.4	0.2	0.2

- Isolation cut efficiency. The comparison of the isolation cut efficiency on $Z \to e^+e^-$ between data and MC, where a relative shift between the mean of the isolation distribution between data and simulation of about 80 MeV is observed, gives an uncertainty of 0.4% (0.5%) per event for $\sqrt{s} = 7(8)$ TeV.

- Event pileup effect. The impact of event pileup on the expected yield is studied by comparing a sample with a mean number of proton-proton interactions of less than 10 (18) with a sample with a mean number of interactions of more than 10 (18) for the $\sqrt{s} = 7(8)$ TeV analysis, and is found to be 4%.

- Photon energy scale. Evaluated as described in Sec. 6.3.2 for the mass shift, the uncertainty in the photon energy scale leads to a 0.3% uncertainty on the $H \to \gamma\gamma$ yield.

- Higgs boson production cross section. The theoretical uncertainties of the Higgs boson production cross section for the different production processes are taken from [47, 67] (see Table 7). The QCD perturbative uncertainties for the gluon fusion process are considered separately for the 2-jets category and the remaining categories (see jet binning below). The uncertainties related to the parton distribution functions are estimated following the prescription in [70] and by using the PDF sets of CTEQ [71], MSTW [72] and NNPDF [73]. They are assumed to be 100% correlated among processes with identical initial states.

- Higgs boson decay branching fraction. The uncertainty on the Higgs boson decay branching fraction to two photons is 5% [74].
- Migration of signal events between categories:
  - Higgs boson kinematics. The uncertainty in the population of the p_{Tt} categories due to the modeling of the Higgs boson kinematics is estimated by varying scales and PDFs used by `HqT2` [47]. This variation leads to an uncertainty on the population of the different categories: 1.1% in the low-p_{T} categories, 12.5% in the high-p_{T} categories, and 9% in the 2-jets category.
  - Event Pileup effects. The impact of pileup on the population of the converted and unconverted categories due to the behavior of the photon reconstruction is studied by comparing a sample with a mean number of interactions of less than 10 (18) with a sample with a mean number of interactions of more than 10 (18) for the $\sqrt{s} = 7(8)$ TeV analysis. The difference in population between the two samples is taken as an estimate of the uncertainty and it is found to be 3% (2%) for categories with unconverted photons, 2% (2%) for categories with converted photons, and 2% (12%) for the 2-jets category, respectively.
  - Material description. The probability for a photon to convert depends on the amount of material it traverses before reaching the calorimeter. The fraction of events in the different categories is compared between the nominal simulation and a simulation sample where additional material amounting to 5% to 20%, depending on the detector region, has been added upstream of the calorimeter. The assigned uncertainty in the signal yield from this source amounts to 4% for categories with unconverted and 3.5% for categories with converted photons.
  - Primary vertex selection. The quantity $\sum p_{\mathrm{T}}^2$, evaluated for signal and background, used for the identification of the primary vertex, has been varied by an amount larger than the difference observed between data and MC. The effect on the expected yield in the different categories is smaller than 0.1% and is neglected.
  - Jet energy scale and resolution. The uncertainties on the jet energy scale is evaluated by varying the scale corrections within their respective uncertainties [27]. The uncertainty for the different classes of categories and different production processes amount to up to 19% for the 2-jets category, and up to 4% for the other categories. The effect on the event yield of varying the jet resolution within its uncertainty is found to be negligible.
  - Jet binning. Following [75] the perturbative uncertainty on the gluon fusion contribution to the 2-jets category is evaluated separately and treated independently from the total cross section uncertainty. It is enhanced in this limited region of phase space due to the presence of higher-order logarithmic contributions. It is found to be 25% on the event yield from the gluon fusion process in the 2-jets category [76].
  - Underlying event. The uncertainty due to the modeling of the underlying event is estimated by comparing different underlying event tunes in the simulation [35]. The `AUET2B` tune is used for the default results, while the `Perugia2011` tune is used for systematic studies. For the 2-jets category, a 30% uncertainty is assigned to the contribution from gluon fusion and the associated production processes, and a 6% uncertainty is assigned to the contribution from vector-boson fusion.
  - Jet-vertex-fraction. The systematic uncertainty on the choice of the jet-vertex-fraction requirement is estimated from the differences of efficiencies between data and MC simulation in $Z + 2jets$ events. For the $\sqrt{s} = 8$ TeV analysis, a 13% uncertainty is assigned.

All systematic uncertainties, except for the uncertainty on the integrated luminosity, are treated as fully correlated between the $\sqrt{s} = 7$ TeV and the $\sqrt{s} = 8$ TeV analyses.

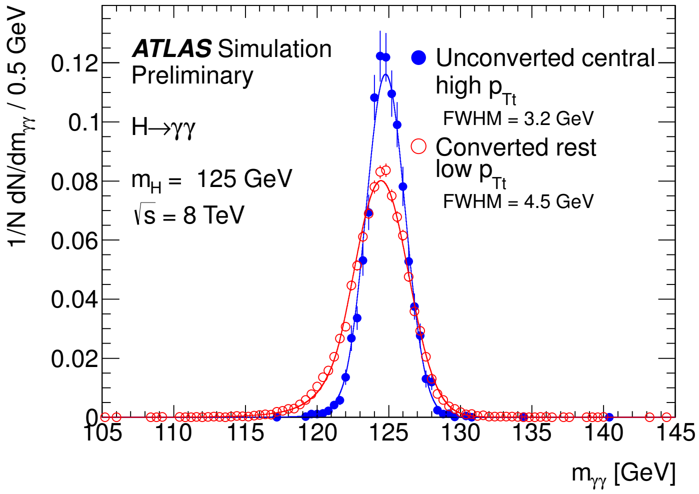

Figure 5: Invariant mass distributions for a Higgs boson with $m_H = 125$ GeV, for the best-resolution category (Unconverted central, high p_{Tt}) shown in blue and for a category with lower resolution (Converted rest, low p_{Tt}) shown in red (see Table 2), for the $\sqrt{s} = 8$ TeV simulation. The invariant mass distribution is parametrized by the sum of a Crystal Ball function and a broad Gaussian, where the latter accounts for fewer than 12% of events in all categories (fewer than 4% in most categories).

6.3 Diphoton mass modeling

The probability density function for the signal is modeled by the sum of a Crystal Ball function (CB) [77] (taking into account the core resolution and a non-Gaussian tail towards lower mass values) and a small, wider Gaussian component (taking into account outliers in the distribution). The CB function is defined as

$$N \cdot \begin{cases} e^{-t^2/2} & \text{if } t > -\alpha \\ \left(\frac{n}{|\alpha|}\right)^n \cdot e^{-|\alpha|^2/2} \cdot \left(\frac{n}{|\alpha|} - |\alpha| - t\right)^{-n} & \text{otherwise} \end{cases} \tag{1}$$

where $t = (m_{\gamma\gamma} - m_H - \delta_{m_H})/\sigma_{CB}$, N is a normalization parameter, m_H is the hypothesized Higgs boson mass, δ_{m_H} is a category dependent offset, σ_{CB} represents the diphoton invariant mass resolution, and n and α parametrize the non-Gaussian tail. Table 2 shows the expected mass resolution for a Higgs boson with $m_H = 126.5$ GeV for the different categories. Fig. 5 shows the resolution function for the categories with the best resolution and another with lower resolution. To extract the parameters from the signal simulation, a simultaneous fit to samples for different Higgs boson masses for each category is performed, exploiting the fact that the shape parameters are either linearly dependent on the Higgs boson mass, or to a good approximation independent of the Higgs boson mass.

6.3.1 Systematic uncertainty on the diphoton mass resolution

The following systematic uncertainties on the invariant mass resolution are considered:

- Uncertainty on the constant term. The parametrization of the calorimeter resolution is described in [12], and includes a constant term and a sampling term. The constant term amounts to about 1% in the calorimeter barrel region and between 1.2% and up to 2.1% in the calorimeter end-caps. It is treated as having an uncertainty as given in [12] and varied within these uncertainties, separately for the parts correlated and uncorrelated with the sampling term. An uncertainty of 12% is assigned to the invariant mass resolution from these variations.

- Electron to photon extrapolation. Assuming that the difference in the calorimeter response to electrons and photons is dominated by the upstream material, the $Z \to e^+e^-$-based inter-calibration is extracted from $Z \to e^+e^-$ simulation samples and applied to $H \to \gamma\gamma$ samples, both with additional material upstream of the calorimeter. This mimics the procedure usually applied to data. The relative uncertainty on the mass resolution obtained is 6%.
- Event pileup effect on energy resolution. The effect of pileup on the mass resolution is studied by comparing the FWHM of the signal peak for events with a mean number of proton-proton interactions of less than 10 (18) with events with a mean number of interactions of more than 10 (18) for the $\sqrt{s} = 7(8)$ TeV analysis. The average observed worsening of the resolution in the higher pileup sample is 4%.
- Primary vertex selection. The quantity $\sum p_{\mathrm{T}}^2$ evaluated for signal and background, used for the identification of the primary vertex, has been varied by an amount larger than the difference observed between data and MC. The effect on the resolution is smaller than 0.2% and is neglected.

The resulting relative uncertainty on the mass resolution is 14%, which is applied to both the Crystal Ball width and the wide Gaussian width in a correlated way. All systematic uncertainties are treated as correlated between the $\sqrt{s} = 7$ TeV and the $\sqrt{s} = 8$ TeV analyses.

6.3.2 Systematic uncertainties due to photon energy scale

The uncertainty on the invariant mass peak position due to the uncertainty on the presampler scale (5% in the barrel, 10% in the end-caps) is evaluated separately for barrel and end-cap candidates. In addition, the uncertainty on the peak position due to material effects when extrapolating the electron energy scale to photons is estimated separately for material volumes before and after $|\eta| = 1.8$. Finally, the effect on the peak position of the multiple small uncertainties generated specifically from the in-situ calibration method is also evaluated. As a result, a 0.6% systematic uncertainty is assigned on the mass scale. The uncertainties are treated as correlated between the $\sqrt{s} = 7$ TeV and $\sqrt{s} = 8$ TeV data.

7 Results

7.1 Background-only fits to the data

The shape parameters and the normalization of the background are determined by a fit to the data events selected in the mass range $100 - 160$ GeV, performed separately for each category and separately for the $\sqrt{s} = 7$ TeV and $\sqrt{s} = 8$ TeV data, using the parametrizations selected in Sec. 5.2. Figs. 6, 7 and 8 show the background-only fits to the data in the different categories for the $\sqrt{s} = 7$ TeV and the $\sqrt{s} = 8$ TeV data. The bottom insets display the residual of the data with respect to the fitted background. The Higgs boson expectation for a mass hypothesis of 126.5 GeV corresponding to the SM cross section is also shown. The inclusive mass distributions of the $\sqrt{s} = 7$ TeV data sample and the $\sqrt{s} = 8$ TeV data sample, along with the background obtained by summing the background-only fits in the individual categories, are shown in Fig. 9. The signal expectation for a SM Higgs boson at $m_H = 126.5$ GeV is overlaid.

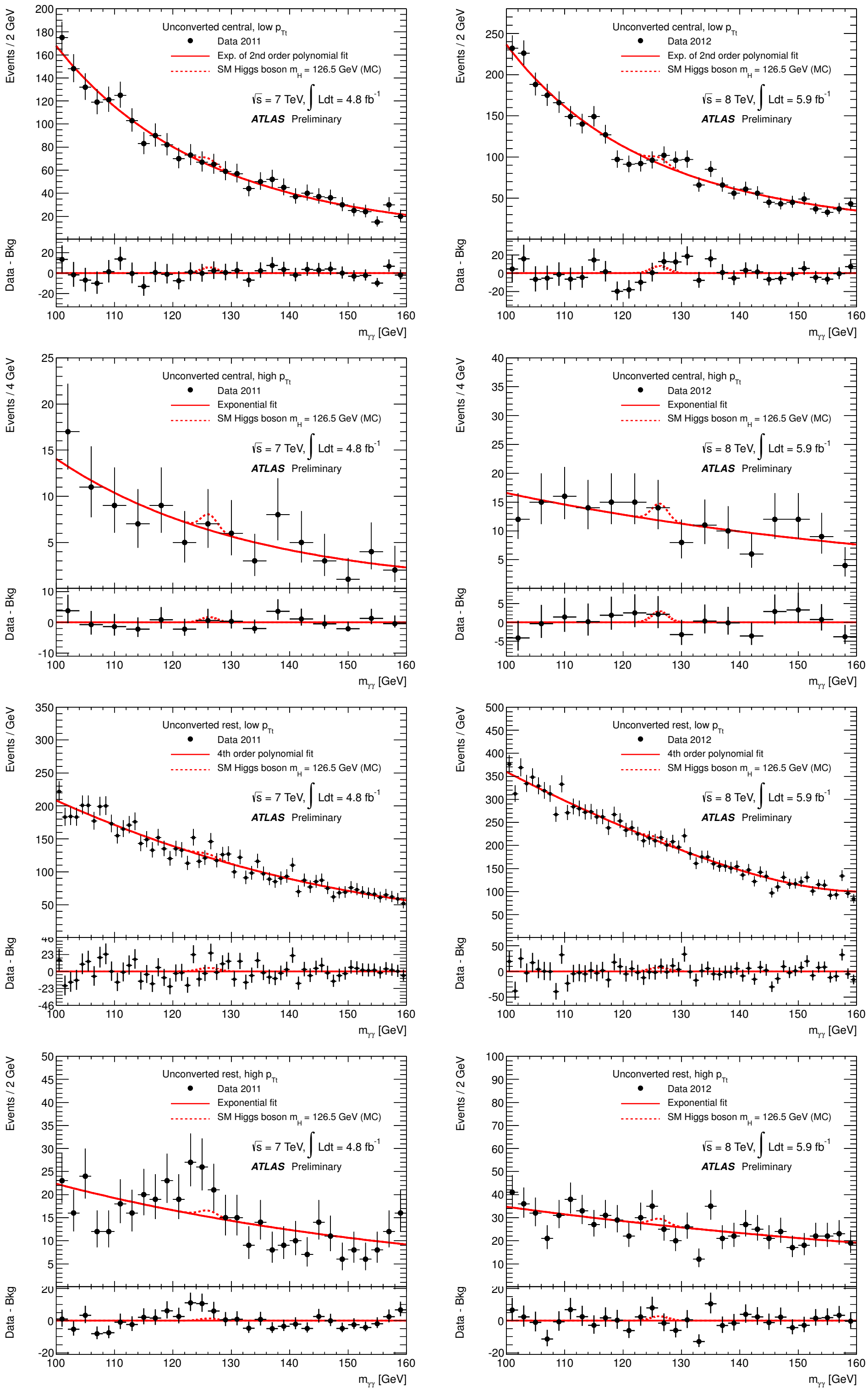

Figure 6: Background-only fits to the diphoton invariant mass spectra for categories Unconverted central, low p_{Tt}, Unconverted central, high p_{Tt}, Unconverted rest, low p_{Tt} and Unconverted rest, high p_{Tt}. The bottom inset displays the residual of the data with respect to the background fit. The Higgs boson expectation for a mass hypothesis of 126.5 GeV corresponding to the SM cross section is also shown. All figures on the left side correspond to the $\sqrt{s}$ = 7 TeV data sample and the ones on the right to the $\sqrt{s}$ = 8 TeV data sample

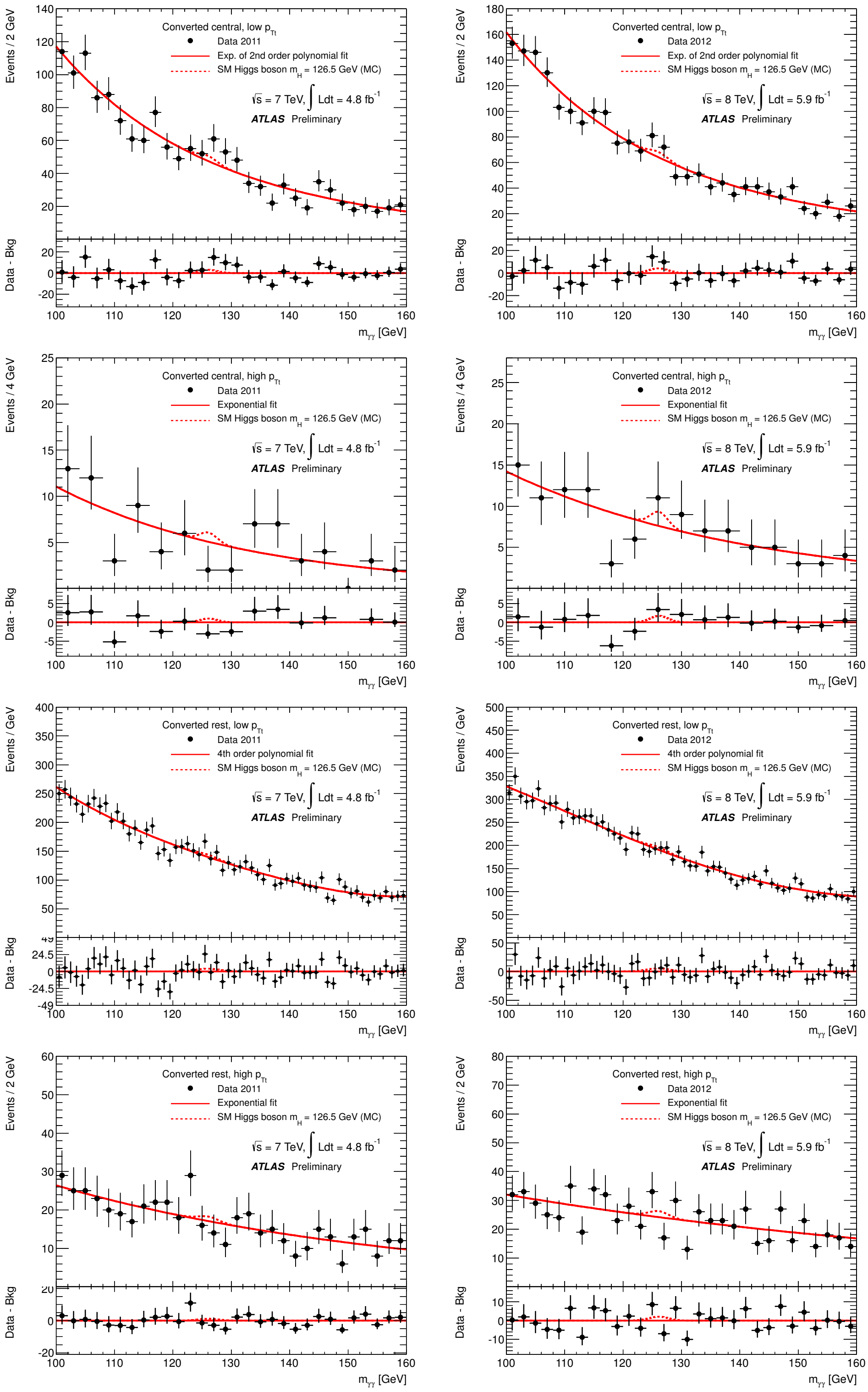

Figure 7: Background-only fits to the diphoton invariant mass spectra for categories Converted central, low p_{Tt}, Converted central, high p_{Tt}, Converted rest, low p_{Tt} and Converted rest, high p_{Tt}. The bottom inset displays the residual of the data with respect to the background fit. The Higgs boson expectation for a mass hypothesis of 126.5 GeV corresponding to the SM cross section is also shown. All figures on the left side show the $\sqrt{s}$ = 7 TeV data sample and the ones on the right show the $\sqrt{s}$ = 8 TeV data sample.

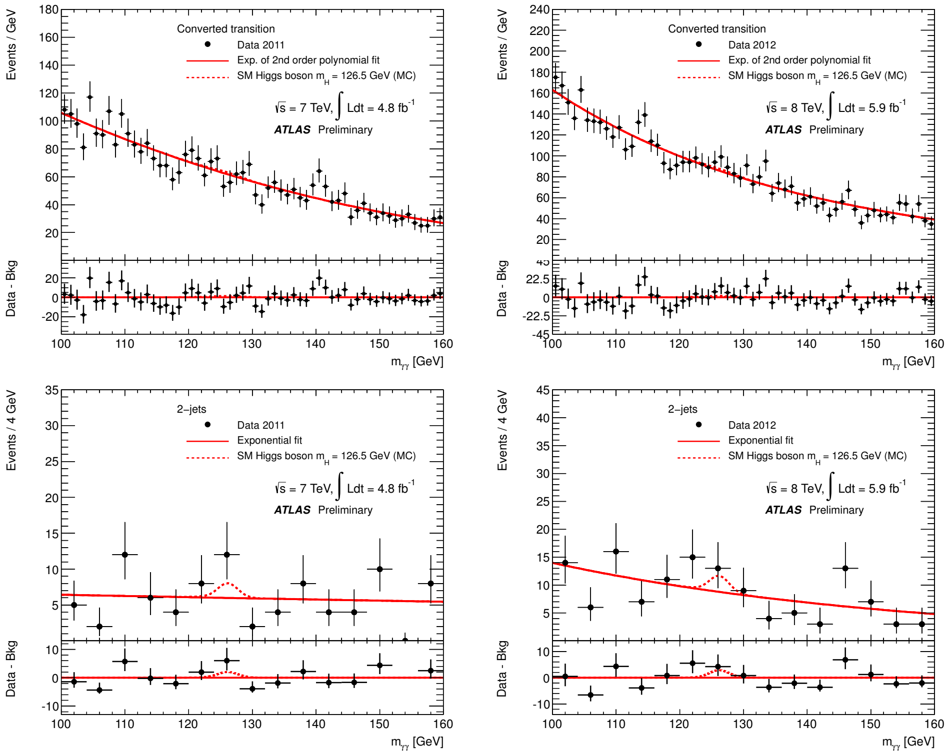

Figure 8: Background-only fits to the diphoton invariant mass spectra for categories Converted transition and 2-jets. The bottom inset displays the residual of the data with respect to the background fit. The Higgs boson expectation for a mass hypothesis of 126.5 GeV corresponding to the SM cross section is also shown. All figures on the left side show the $\sqrt{s}$ = 7 TeV data sample and the ones on the right show the $\sqrt{s}$ = 8 TeV data sample.

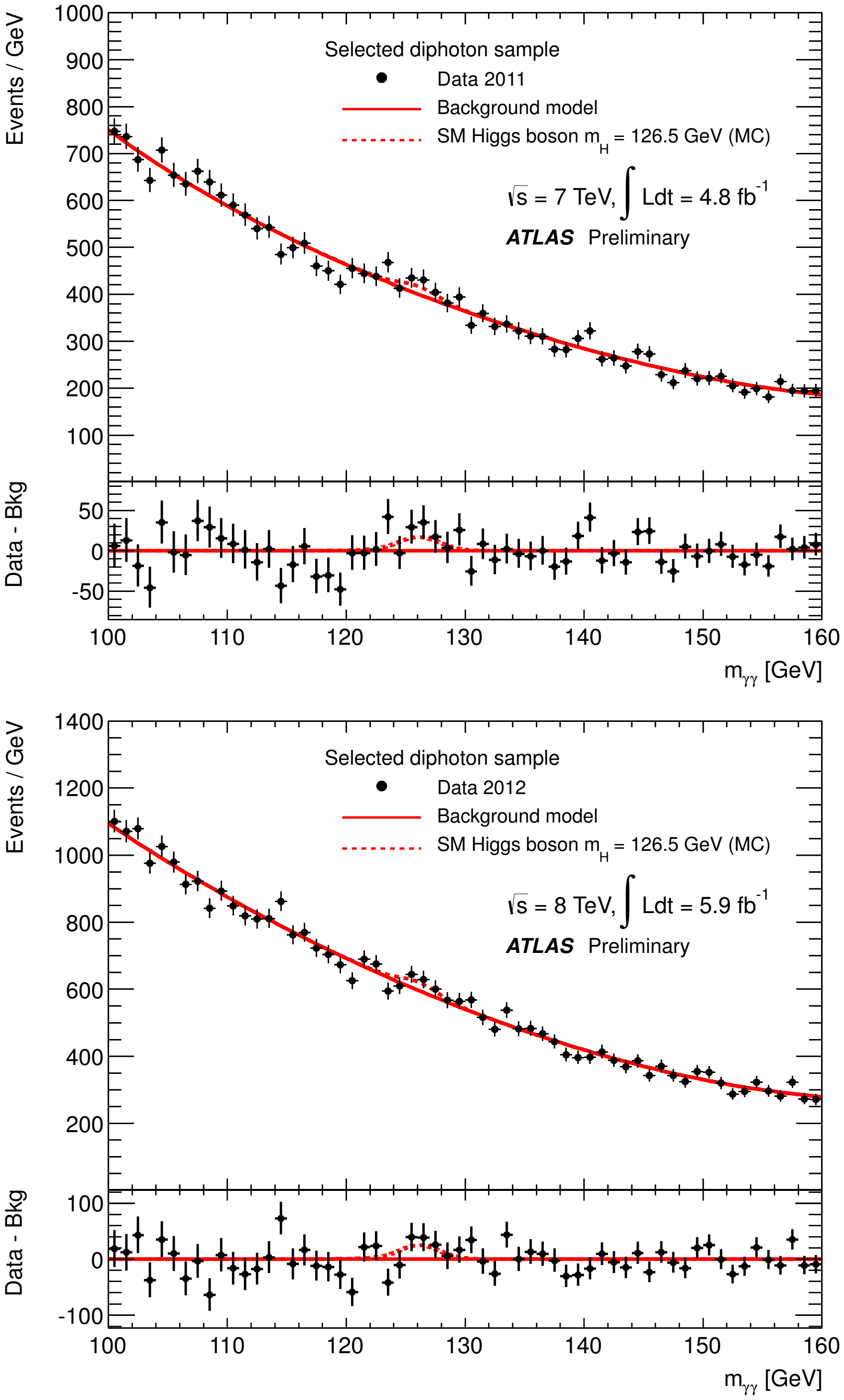

Figure 9: Invariant mass distribution for the selected $\sqrt{s}$ = 7 TeV (top) and $\sqrt{s}$ = 8 TeV (bottom) data sample, overlaid with the total background obtained from summing the fitted background distributions in the individual categories. The bottom inset displays the residual of the data with respect to the total background. The Higgs boson expectation for a mass hypothesis of 126.5 GeV corresponding to the SM cross section is also shown.

7.2 Comparison to background-only hypothesis and exclusion limits

The statistical procedures used to test the background-only hypothesis and to set exclusion limits are described in detail in [78]. These take the form of statistical tests of different hypothesized values of a strength parameter μ, defined as the ratio of the signal rate (cross section) being tested to that predicted by the SM. That is, $\mu = 0$ is the background-only hypothesis and $\mu = 1$ is the SM hypothesis. At fixed values of the Higgs boson mass m_H, different values of μ are tested using a statistic based on the profile likelihood ratio. This statistic depends on the parameter of interest μ as well as nuisance parameters that characterize the systematic uncertainties described above. Exclusion limits on the Higgs boson production cross section for the decay into two photons are determined using the CL_s procedure [79] at 95% confidence level (CL). To quantify discovery significance, the p-value of the background-only hypothesis, p_0, is reported. Equivalently, this can be expressed using the discovery significance $Z_0 = \Phi^{-1}(1 - p_0)$, where Φ^{-1} is the standard Gaussian quantile. The p-value is extracted from the distribution of the profile likelihood ratio using the asymptotic approximation [80]. The systematic uncertainties are taken into account in the limit by incorporating probability distribution functions that constrain the uncertainties in the likelihood function. The different sources of systematic uncertainties and their values are summarized in Table 7. They are treated as fully correlated between the $\sqrt{s} = 7$ TeV and $\sqrt{s} = 8$ TeV analyses, with the exception of the systematic uncertainty from the luminosity measurement. The impact of the photon energy scale on the mass position is excluded from this procedure and evaluated instead using a procedure based on pseudo-experiments [6]. The invariant mass distribution of the background is modeled as described in Sec. 5.

The compatibility of the selected events with the background-only hypothesis is quantified by the background-only p_0. The minimal p_0-values observed in the mass range 110 – 150 GeV for the $\sqrt{s} = 7$ TeV and the $\sqrt{s} = 8$ TeV data samples are 2.8×10^{-4} and 3.1×10^{-4}, respectively. They are found at $m_H = 126$ GeV and 127 GeV and correspond to local significances of 3.5σ and 3.4σ. For a SM Higgs boson, the expected p_0 values would be 6×10^{-2} and 3×10^{-2} at these hypothesized mass values, corresponding to local significances of 1.6σ and 1.9σ, respectively. The positions of the two minima are compatible within their uncertainties. To correct the local significances for the look-elsewhere effect, the approximate procedure of [81] is used. The global significance is 2.2σ for the $\sqrt{s} = 7$ TeV as well as for the $\sqrt{s} = 8$ TeV sample, when the energy scale uncertainty has been taken into account.

The results obtained with the $\sqrt{s} = 7$ TeV data sample and the $\sqrt{s} = 8$ TeV data sample are combined statistically. The combined p_0-value is shown in Fig. 10, along with the p_0 for the $\sqrt{s} = 7$ TeV and the $\sqrt{s} = 8$ TeV analyses. The minimal p_0-value observed is 2×10^{-6} at $m_H = 126.5$ GeV and corresponds to a local significance of 4.7σ. This is reduced to 4.5σ when taking the energy scale systematic uncertainty into account. After correction for the look-elsewhere effect, a global significance of 3.6σ is found. At this hypothesized mass, the expected p_0 value for a SM Higgs boson is 7×10^{-3} (2.4σ local significance).

As a cross-check, the analysis is repeated without dividing the datasets into categories. The observed (expected) p_0 values are found to be 3×10^{-3} (0.1) and 5×10^{-3} (0.1) for the $\sqrt{s} = 7$ TeV and $\sqrt{s} = 8$ TeV data, respectively. This corresponds to a local significance of 2.7σ and 2.6σ, respectively. For the combined $\sqrt{s} = 7$ TeV and $\sqrt{s} = 8$ TeV analysis, the observed (expected) p_0 value is found to be 2×10^{-4} (0.03). This corresponds to a local significance of 3.5σ. The corresponding p_0 distribution is shown in Fig. 11 and also compared the analysis without the 2-jets category.

Results for 95% CL exclusions on the Higgs boson production cross section are obtained in the mass range 110 – 150 GeV. The expected CL_s limit for SM background without a Higgs boson ranges from 1.3 to 2.5 times the SM expectation in the considered mass range in the $\sqrt{s} = 7$ TeV data. For the $\sqrt{s} = 8$ TeV data, the expected CL_s limit ranges from 1.1 to 2.1 times the SM expectation in the considered mass range. A SM Higgs boson is excluded in the mass range of (113 – 121) GeV in the $\sqrt{s} = 7$ TeV data sample and in the range (118 – 123) GeV and (138 – 142) GeV in the $\sqrt{s} = 8$ TeV data sample. Results for the combined $\sqrt{s} = 7$ TeV and $\sqrt{s} = 8$ TeV analysis are shown in Fig. 12.

Table 7: Summary of systematic uncertainties on the expected signal and the background. The values given are the relative uncertainties on these quantities from the various sources investigated for a Higgs boson mass of 125 GeV, except for the case of background modeling, where the uncertainties are provided in Table 3 in terms of the number of events. The sign in the front of values for each systematic uncertainty shows correlations among categories and processes.

Systematic uncertainties	$\sqrt{s}$ = 7 TeV [%]	$\sqrt{s}$ = 8 TeV [%]
Signal event yield		
Photon identification	±8.4	±10.8
Effect of pileup on photon rec/ID	±4	
Photon energy scale	±0.3	
Photon Isolation	±0.4	±0.5
Trigger	±1	
Higgs boson cross section (perturbative)	$gg \to H$: $^{+12}_{-8}$, VBF: ±0.3, WH: $^{+0.2}_{-0.8}$, ZH: $^{+1.4}_{-1.6}$, ttH: $^{+3}_{-9}$	$gg \to H$: $^{+7}_{-8}$, VBF: ±0.2, WH: $^{+0.2}_{-0.6}$, ZH: $^{+1.6}_{-1.5}$, ttH: $^{+4}_{-9}$
	$gg \to H + 2$ jets: ±25	
Higgs boson cross section (PDF+α_S)	$gg \to H$: $^{+8}_{-7}$, VBF: $^{+2.5}_{-2.1}$, VH: ±3.5, ttH: ±9	$gg \to H$: $^{+8}_{-7}$, VBF: $^{+2.6}_{-2.8}$, VH: ±3.5, ttH: ±8
Higgs boson branching ratio	±5	
Higgs boson p_{T} modeling	low p_{Tt}: ±1.1, high p_{Tt}: ∓12.5, 2-jets: ∓9	
Underlying Event (2-jets)	VBF: ±6, Others: ±30	
Luminosity	±1.8	±3.6
Signal category migration		
Material	Unconv: ±4, Conv: ∓3.5	
Effect of pileup on photon rec/ID	Unconv: ±3, Conv: ∓2, 2-jets: ±2	Unconv: ±2, Conv: ∓2, 2-jets: ±12
Jet energy scale	low p_{Tt}	
	$gg \to H$: ±0.1, VBF: ±2.6, Others: ±0.1	$gg \to H$: ±0.1, VBF: ±2.3, Others: ±0.1
	high p_{Tt}	
	$gg \to H$: ±0.1, VBF: ±4, Others: ±0.1	$gg \to H$: ±0.1, VBF: ±4, Others: ±0.1
	2-jets	
	$gg \to H$: ∓19, VBF: ∓8, Others: ∓15	$gg \to H$: ∓18, VBF: ∓9, Others: ∓13
Jet-vertex-fraction		2-jets: ±13, Others: ∓0.3
Primary vertex selection	negligible	
Signal mass resolution		
Calorimeter energy resolution	±12	
Electron to photon extrapolation	±6	
Effect of pileup on energy resolution	±4	
Primary vertex selection	negligible	
Signal mass position		
Photon energy scale	±0.6	
Background modeling	see Table 3	

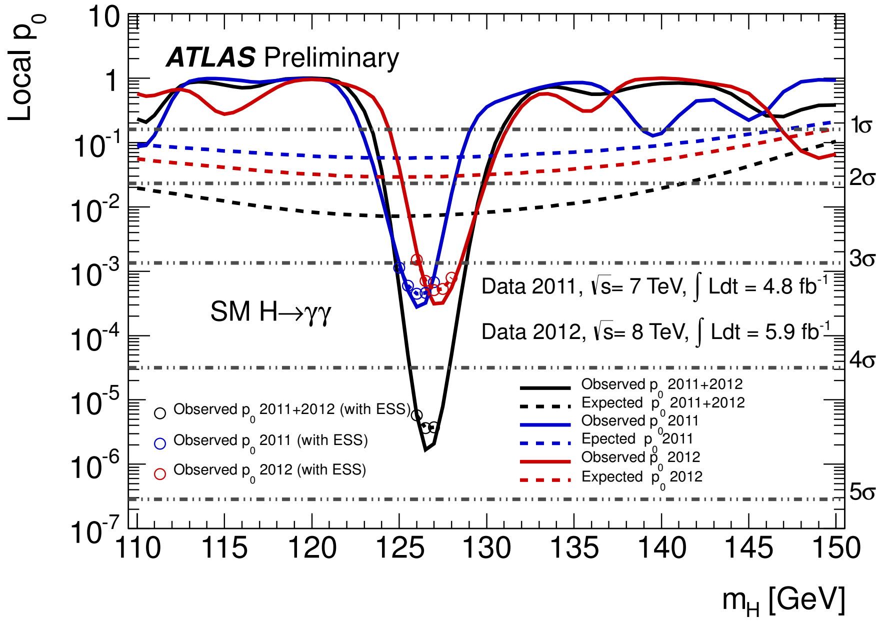

Figure 10: Expected and observed local p_0 values for a SM Higgs boson as a function of the hypothesized Higgs boson mass (m_H) for the combined analysis and for the $\sqrt{s}$ = 7 TeV and $\sqrt{s}$ = 8 TeV data samples separately. The observed p_0 including the effect of the photon energy scale uncertainty on the mass position is included via pseudo-experiments and shown as open circles.

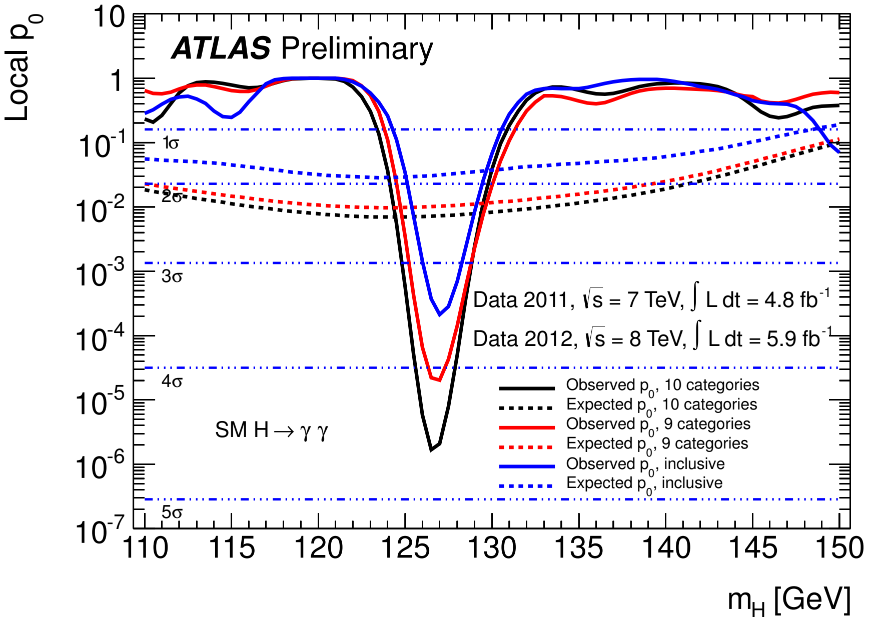

Figure 11: Expected and observed local p_0 for the analysis using 10 categories, compared to an analysis using only 9 categories (no 2-jets category) and a fully inclusive analysis for the combined $\sqrt{s}$ = 7 TeV and $\sqrt{s}$ = 8 TeV data.

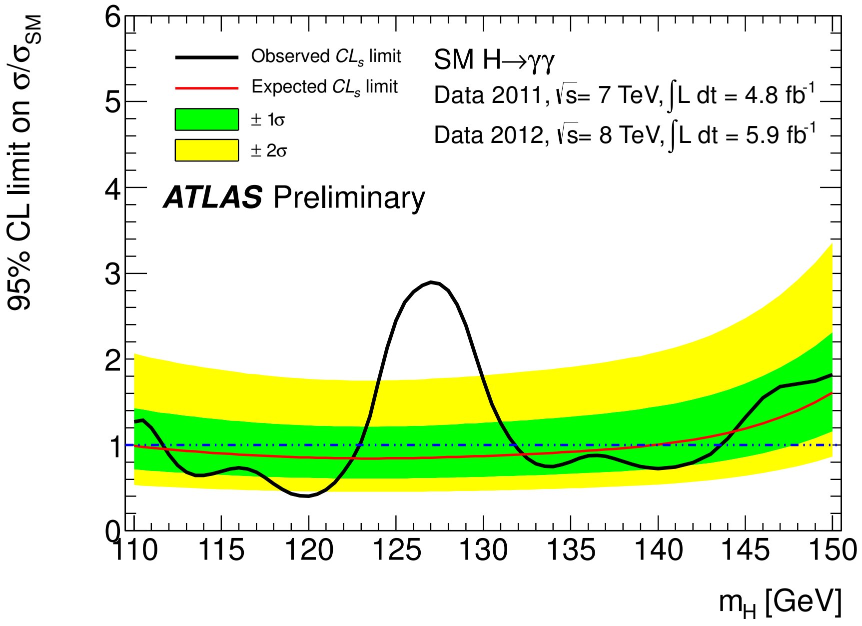

Figure 12: Expected and observed CL_s limit on the normalized signal strength as a function of the assumed Higgs boson mass for the combined analysis.

The expected CL_s limit ranges from 0.8 to 1.6 times the SM expectation in the considered mass range. Under the background-only assumption, the expected range for the exclusion of a SM Higgs boson is (110.0 – 139.5) GeV. A SM Higgs boson is excluded in the mass ranges of (112 – 122.5) GeV and (132 – 143) GeV.

The best fit value for the signal strength μ is obtained from a simultaneous fit to all categories in the $\sqrt{s}$ = 7 TeV and $\sqrt{s}$ = 8 TeV data samples. For every mass point, the signal shape parameters are fixed by the procedure described in Sec. 6 and a common signal strength parameter is fitted along with the nuisance parameters for the systematic uncertainties. The result is shown in Fig. 13. At m_H = 126.5 GeV, the best fit value is $\hat{\mu} = 1.9 \pm 0.5$, which correspond to about 360 signal events. The best fit value for the signal strength at m_H = 126.5 GeV obtained from fits to the individual categories is shown in Fig. 14.

As a result of quantifying the best fit value at the point of largest deviation from the background-only hypothesis, a positive bias on $\hat{\mu}$ is expected. The bias has been evaluated with pseudo-experiments and has been found to be around 8%.

Fig. 15 shows the invariant mass of diphoton candidates in the combined $\sqrt{s}$ = 7 TeV and $\sqrt{s}$ = 8 TeV data samples, and the result of a fit with a SM Higgs boson signal fixed at m_H = 126.5 GeV and a background component.

The second most significant deviation from the background-only hypothesis is a deficit of events around 120 GeV. This deficit has a local significance of 2.6σ, which corresponds to 1.2σ with look-elsewhere effect taken into account. All other observed deviations are less than 1.5σ in local significance.

The results presented so far do not give precise information about the range of masses consistent with a potential signal, because the statistical procedure is performed in a scan over m_H with m_H fixed in the likelihood as if it were known a priori. This shortcoming can be addressed by considering various contours of the likelihood function.

In order to address the values of the signal strength and mass of a potential signal that are simultane-

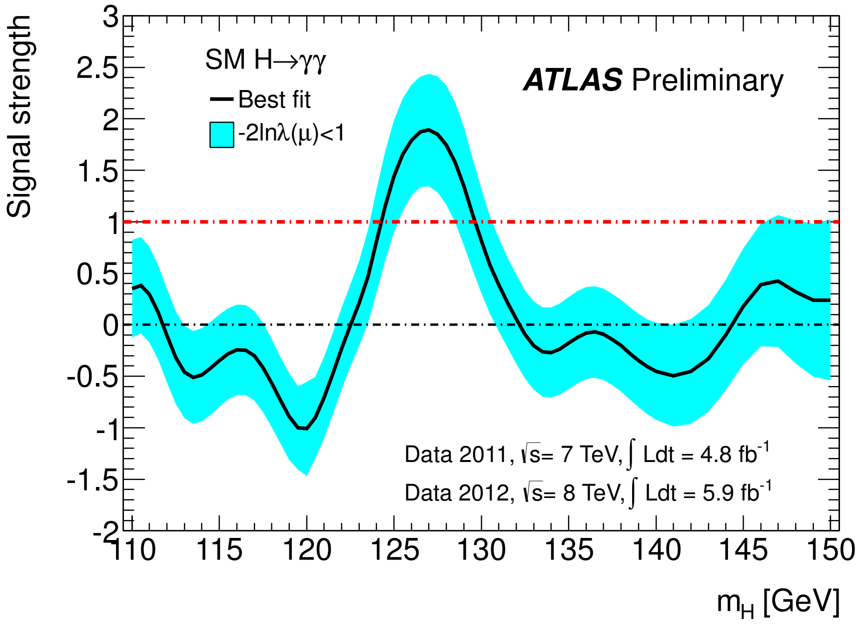

Figure 13: Best fit value for the signal strength as a function of the assumed Higgs boson mass for the combined analysis.

ously consistent with the data, the following profile likelihood ratio is appropriate:

$$\lambda(\mu, m_H) = \frac{L(\mu, m_H, \hat{\hat{\vec{\theta}}}(\mu, m_H))}{L(\hat{\mu}, \hat{m}_H, \hat{\vec{\theta}})}, \tag{2}$$

where $\hat{\hat{\vec{\theta}}}(\mu, m_H)$ is the conditional maximum likelihood estimate with μ and m_H fixed. In the presence of a strong signal, this test statistic will produce closed contours about the best fit point $(\hat{\mu}, \hat{m}_H)$, while a mild excess will produce an upper-limit on $\hat{\mu}$ for all values of m_H. Asymptotically, the test statistic $-2 \ln \lambda(\mu, m_H)$ is distributed as a χ^2 distribution with two degrees of freedom. The expected asymptotic distribution was explicitly checked with ensembles of pseudo-experiments. In particular, the $100(1-\alpha)\%$ confidence level contours are defined by $-2 \ln \lambda(\mu, m_H) < k_\alpha$, where k_α satisfies $P(\chi_2^2 > k_\alpha) = \alpha$. The obtained likelihood contours in the (μ, m_H) plane are shown in Fig. 16 and correspond to 68% and 95% CL contours.

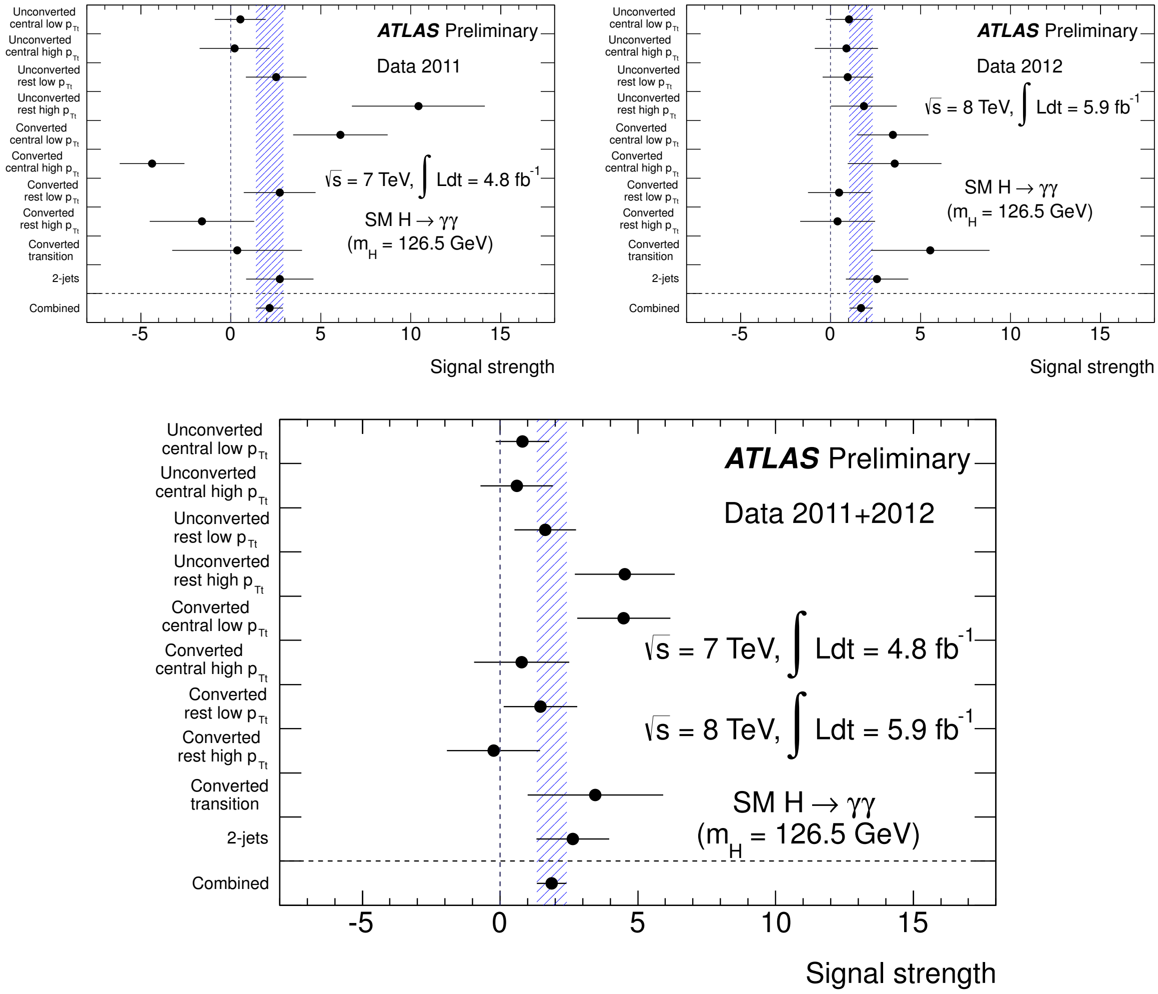

Figure 14: Best fit value for the signal strength in the different categories at m_H = 126.5 GeV for the $\sqrt{s}$ = 7 TeV (left) and the $\sqrt{s}$ = 8 TeV (right) data sample (top) and for the combined $\sqrt{s}$ = 7 TeV and $\sqrt{s}$ = 8 TeV data samples (bottom).

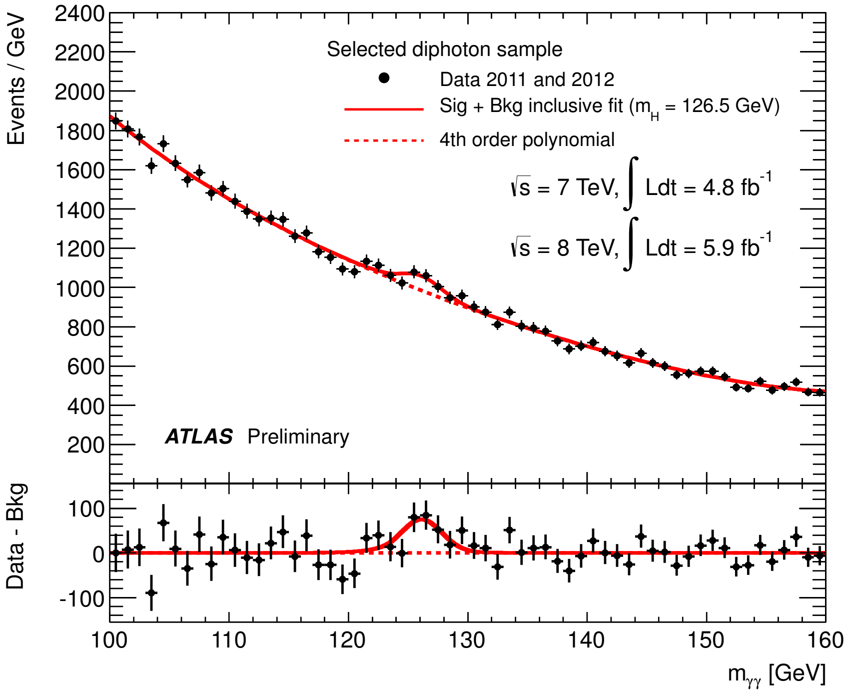

Figure 15: Invariant mass distribution for the combined $\sqrt{s}$ = 7 TeV and $\sqrt{s}$ = 8 TeV data samples. Superimposed is the result of a fit including a signal component fixed to a hypothesized mass of 126.5 GeV and a background component described by a fourth-order Bernstein polynomial. The bottom inset displays the residual of the data with respect to the fitted background.

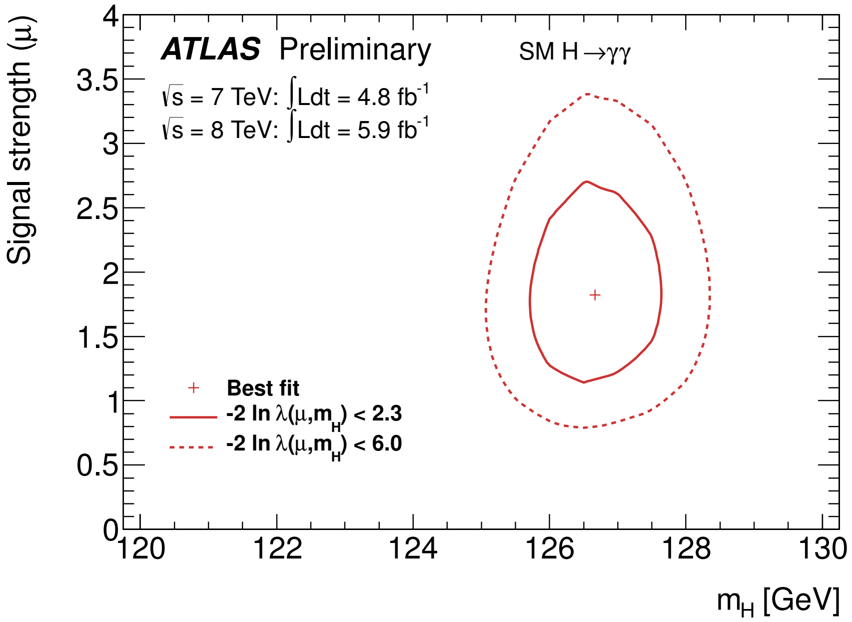

Figure 16: Likelihood contours in the (μ, m_H) plane. The contours are for the combined $\sqrt{s} = 7$ TeV and $\sqrt{s} = 8$ TeV analysis and correspond to 68% and 95% CL contours.

8 Conclusions

This note summarizes the search for the SM Higgs boson in the diphoton decay channel in proton-proton collisions for an integrated luminosity of 4.8 fb^{-1} at a center-of-mass energy of $\sqrt{s} = 7$ TeV and 5.9 fb^{-1} at a center-of-mass energy of $\sqrt{s} = 8$ TeV, recorded with the ATLAS detector at the Large Hadron Collider.

Exclusion limits are set with the CL_s approach and the expected exclusions range from 0.8 to 1.6 times the SM Higgs boson production cross section, in the Higgs boson mass range (110 − 150) GeV, and result in an expected exclusion range from 110 GeV to 139.5 GeV. The observed exclusion ranges for a SM Higgs boson are (112 − 122.5) GeV and (132 − 143) GeV at 95% CL.

An excess over the expected background is observed around 126.5 GeV and corresponds to a local significance of 4.5σ.

References

[1] F. Englert and R. Brout, *Broken symmetry and the mass of gauge vector mesons*, Phys. Rev. Lett. **13** (1964) 321–323.

[2] P. W. Higgs, *Broken symmetries and the masses of gauge bosons*, Phys. Rev. Lett. **13** (1964) 508–509.

[3] G. Guralnik, C. Hagen, and T. Kibble, *Global conservation laws and massless particles*, Phys. Rev. Lett. **13** (1964) 585–587.

[4] LEP Working Group for Higgs boson searches, ALEPH Collaboration, DELPHI Collaboration, L3 Collaboration, OPAL Collaboration, R. Barate et al., *Search for the standard model Higgs boson at LEP*, Phys. Lett. **B565** (2003) 61–75, `arXiv:hep-ex/0306033 [hep-ex]`.

[5] TEVNPH (Tevatron New Phenomina and Higgs Working Group), CDF Collaboration, D0 Collaboration Collaboration, *Combined CDF and D0 Search for Standard Model Higgs Boson Production with up to 10.0* fb^{-1} *of Data*, `arXiv:1203.3774 [hep-ex]`.

[6] The ATLAS Collaboration, *An update to the combined search for the Standard Model Higgs boson with the ATLAS detector at the LHC using up to* 4.9fb^{-1} *of pp collision data at* $\sqrt{s} = 7$ TeV, ATLAS-CONF-2012-019 (2012) .

[7] CMS Collaboration, *Combined results of searches for a Higgs boson in the context of the standard model and beyond-standard models*, CMS PAS HIG-12-008 (2012) .

[8] The ATLAS Collaboration, *Search for the Standard Model Higgs boson in the diphoton decay channel with* 4.9fb^{-1} *of pp collision data at* $\sqrt{s} = 7$ TeV *with ATLAS*, Phys. Rev. Lett. **108** (2012) 111803, `arXiv:1202.1414 [hep-ex]`.

[9] CMS Collaboration, *Search for the standard model Higgs boson decaying into two photons in pp collisions at* $\sqrt{s} = 7$ TeV, Phys. Lett. **B710** (2012) 403–425, `arXiv:1202.1487 [hep-ex]`.

[10] The ATLAS Collaboration, *The ATLAS experiment at the CERN Large Hadron Collider*, JINST **3** (2008) S08003.

[11] The ATLAS Collaboration, *Expected photon performance in the ATLAS experiment*, ATLAS-PHYS-PUB-2011-007 (2011) .

[12] The ATLAS Collaboration, *Electron performance measurements with the ATLAS detector using the 2010 LHC proton-proton collision data*, Eur. Phys. J. **C72** (2012) 1909, `arXiv:1110.3174 [hep-ex]`.

[13] W. Lampl et al., *Calorimeter clustering algorithms: description and performance*, Tech. Rep. ATL-LARG-PUB-2008-002, 2008.

[14] S. D. Ellis and D. E. Soper, *Successive combination jet algorithm for hadron collisions*, Phys. Rev. **D48** (1993) 3160–3166, `arXiv:hep-ph/9305266 [hep-ph]`.

[15] S. Catani, Y. L. Dokshitzer, M. Seymour, and B. Webber, *Longitudinally invariant* K_t *clustering algorithms for hadron hadron collisions*, Nucl. Phys. **B406** (1993) 187–224.

[16] The ATLAS Collaboration, *Measurement of the inclusive isolated prompt photon cross section in pp collisions at* $\sqrt{s} = 7$ TeV *with the ATLAS detector*, Phys. Rev. **D83** (2011) 052005, `arXiv:1012.4389 [hep-ex]`.

[17] The ATLAS Collaboration, *Performance of the ATLAS Trigger System in 2010*, Eur. Phys. J. **C72** (2012) 1849, `arXiv:1110.1530 [hep-ex]`.

[18] The ATLAS Collaboration, *Expected performance of the ATLAS experiment: detector, trigger and physics*, CERN-OPEN-2008-020 (2008) .

[19] The OPAL Collaboration, *Search for Anomalous Production of Di-lepton Events with Missing Transverse Momentum in* e^+e^- *Collisions at* $\sqrt{s} = 161$ *and 172 GeV*, Eur. Phys. J. **C4** (1998) 47–74.

[20] M. Vesterinen and T. R. Wyatt, *A Novel Technique for Studying the Z Boson Transverse Momentum Distribution at Hadron Colliders*, Nucl. Instrum. Meth. **A602** (2009) 432–437.

[21] T. Gleisberg, S. Hoeche, F. Krauss, M. Schonherr, S. Schumann, et al., *Event generation with SHERPA 1.1*, JHEP **0902** (2009) 007, `arXiv:0811.4622 [hep-ph]`.

[22] M. L. Mangano et al., *ALPGEN, a generator for hard multiparton processes in hadronic collisions*, JHEP **07** (2003) 001.

[23] M. Cacciari, G. P. Salam, and G. Soyez, *The Anti-k(t) jet clustering algorithm*, JHEP **0804** (2008) 063, `arXiv:0802.1189 [hep-ph]`.

[24] C. Cojocaru et al., *Hadronic calibration of the ATLAS liquid argon end-cap calorimeter in the pseudorapidity region* $1.6 < |\eta| < 1.8$ *in beam tests*, Nucl. Instrum. Meth. **A 531** (2004) 481–514.

[25] The ATLAS Collaboration, *Jet energy measurement with the ATLAS detector in proton-proton collisions at* $\sqrt{s} = 7$ TeV , Submitted to EPJ (2011) , `arXiv:1112.6426 [hep-ex]`.

[26] The ATLAS Collaboration, *Pile-up corrections for jets from proton-proton collisions at* $\sqrt{s} = 7$ TeV *in ATLAS in 2011*, Tech. Rep. ATLAS-CONF-2012-064, 2012.

[27] The ATLAS Collaboration, *Jet energy measurement with the ATLAS detector in proton-proton collisions at* $\sqrt{s} = 7$ TeV, `arXiv:1112.6426 [hep-ex]`.

[28] The ATLAS Collaboration, *Search for the Standard Model Higgs boson in the diphoton decay channel with* $4.9\,\text{fb}^{-1}$ *of ATLAS data at* $\sqrt{s} = 7$ TeV, ATLAS-CONF-2011-161 (2011) .

[29] The ATLAS Collaboration, *Measurement of the isolated di-photon cross-section in pp collisions at* $\sqrt{s} = 7$ TeV *with the ATLAS detector*, Phys. Rev. **D85** (2012) 012003, `arXiv:1107.0581 [hep-ex]`.

[30] C. Balazs, E.L. Berger, P.M. Nadolsky, and C.P. Yuan, *Calculation of prompt diphoton production cross-sections at Tevatron and LHC energies*, Phys. Rev. **D76** (2007) 013009.

[31] T. Binoth, J. Guillet, E. Pilon, and M. Werlen, *A full next-to-leading order study of direct photon pair production in hadronic collisions*, Eur. Phys. J. **C16** (2000) 311.

[32] T. Sjöstrand, S. Mrenna, P. Skands, *PYTHIA 6.4 physics and manual*, JHEP **05** (2006) 026.

[33] The ATLAS Collaboration, *The ATLAS simulation infrastructure*, Eur. Phys. J. **C70** (2010) 823–874.

[34] GEANT4 Collaboration, S. Agostinelli et al., *GEANT4: A simulation toolkit*, Nucl. Instrum. Meth. **A506** (2003) 250–303.

[35] The ATLAS Collaboration, *ATLAS tunes of PYTHIA 6 and Pythia 8 for MC11*, ATL-PHYS-PUB-2011-009, online at https://cdsweb.cern.ch/record/1363300 (2011) .

[36] S. Alioli, P. Nason, C. Oleari and E. Re, *NLO Higgs boson production via gluon fusion matched with shower in POWHEG*, JHEP **04** (2009) 002.

[37] P. Nason and C. Oleari, *NLO Higgs boson production via vector-boson fusion matched with shower in POWHEG*, JHEP **02** (2010) 037.

[38] T. Sjöstrand, S. Mrenna, P. Skands, *A brief introduction to PYTHIA 8.1*, Comput.Phys.Commun. **178** (2008) 852–867.

[39] A. Djouadi, M. Spira, and P. Zerwas, *Production of Higgs bosons in proton colliders: QCD corrections*, Phys. Lett. **B264** (1991) 440–446.

[40] S. Dawson, *Radiative corrections to Higgs boson production*, Nucl. Phys. **B359** (1991) 283–300.

[41] M. Spira, A. Djouadi, D. Graudenz, and P. Zerwas, *Higgs boson production at the LHC*, Nucl. Phys. **B453** (1995) 17–82, `arXiv:hep-ph/9504378 [hep-ph]`.

[42] R. V. Harlander and W. B. Kilgore, *Next-to-next-to-leading order Higgs production at hadron colliders*, Phys. Rev. Lett. **88** (2002) 201801, `arXiv:hep-ph/0201206 [hep-ph]`.

[43] C. Anastasiou and K. Melnikov, *Higgs boson production at hadron colliders in NNLO QCD*, Nucl. Phys. **B646** (2002) 220–256, `arXiv:hep-ph/0207004 [hep-ph]`.

[44] V. Ravindran, J. Smith, and W. L. van Neerven, *NNLO corrections to the total cross-section for Higgs boson production in hadron hadron collisions*, Nucl. Phys. **B665** (2003) 325–366, `arXiv:hep-ph/0302135 [hep-ph]`.

[45] S. Catani, D. de Florian, M. Grazzini, and P. Nason, *Soft gluon resummation for Higgs boson production at hadron colliders*, JHEP **0307** (2003) 028, `arXiv:hep-ph/0306211 [hep-ph]`.

[46] D. de Florian, G. Ferrera, M. Grazzini, and D. Tommasini, *Transverse-momentum resummation: Higgs boson production at the Tevatron and the LHC*, JHEP **1111** (2011) 064, `arXiv:1109.2109 [hep-ph]`.

[47] LHC Higgs Cross Section Working Group, S. Dittmaier, C. Mariotti, G. Passarino, and R. Tanaka (Eds.), *Handbook of LHC Higgs Cross Sections: 2. Differential Distributions*, CERN-2012-002 (CERN, Geneva, 2012) , `arXiv:1201.3084 [hep-ph]`.

[48] U. Aglietti, R. Bonciani, G. Degrassi, and A. Vicini, *Two loop light fermion contribution to Higgs production and decays*, Phys. Lett. **B595** (2004) 432–441, `arXiv:hep-ph/0404071 [hep-ph]`.

[49] S. Actis, G. Passarino, C. Sturm, and S. Uccirati, *NLO electroweak corrections to Higgs boson production at hadron colliders*, Phys. Lett. **B670** (2008) 12–17, `arXiv:0809.1301 [hep-ph]`.

[50] D. de Florian and M. Grazzini, *Higgs production at the LHC: updated cross sections at* $\sqrt{s} = 8$ *TeV*, `arXiv:1206.4133 [hep-ph]`.

[51] C. Anastasiou, S. Buehler, F. Herzog, and A. Lazopoulos, *Inclusive Higgs boson cross-section for the LHC at 8 TeV*, JHEP **1204** (2012) 004, `arXiv:1202.3638 [hep-ph]`.

[52] J. Baglio and A. Djouadi, *Higgs production at the lHC*, JHEP **1103** (2011) 055, `arXiv:1012.0530 [hep-ph]`.

[53] M. Ciccolini, A. Denner, and S. Dittmaier, *Strong and electroweak corrections to the production of Higgs + 2-jets via weak interactions at the LHC*, Phys. Rev. Lett. **99** (2007) 161803, `arXiv:0707.0381 [hep-ph]`.

[54] M. Ciccolini, A. Denner, and S. Dittmaier, *Electroweak and QCD corrections to Higgs production via vector-boson fusion at the LHC*, Phys. Rev. **D77** (2008) 013002, `arXiv:0710.4749 [hep-ph]`.

[55] K. Arnold, M. Bahr, G. Bozzi, F. Campanario, C. Englert, et al., *VBFNLO: A Parton level Monte Carlo for processes with electroweak bosons*, Comput. Phys. Commun. **180** (2009) 1661–1670, `arXiv:0811.4559 [hep-ph]`.

[56] P. Bolzoni, F. Maltoni, S.-O. Moch, and M. Zaro, *Higgs production via vector-boson fusion at NNLO in QCD*, Phys. Rev. Lett. **105** (2010) 011801, `arXiv:1003.4451 [hep-ph]`.

[57] T. Han and S. Willenbrock, *QCD correction to the* $pp \rightarrow WH$ *and ZH total cross-sections*, Phys. Lett. **B273** (1991) 167–172.

[58] O. Brein, A. Djouadi, and R. Harlander, *NNLO QCD corrections to the Higgs-strahlung processes at hadron colliders*, Phys. Lett. **B579** (2004) 149–156, `arXiv:hep-ph/0307206 [hep-ph]`.

[59] M. Ciccolini, S. Dittmaier, and M. Krämer, *Electroweak radiative corrections to associated WH and ZH production at hadron colliders*, Phys. Rev. **D68** (2003) 073003, `arXiv:hep-ph/0306234 [hep-ph]`.

[60] W. Beenakker, S. Dittmaier, M. Kramer, B. Plumper, M. Spira, et al., *Higgs radiation off top quarks at the Tevatron and the LHC*, Phys. Rev. Lett. **87** (2001) 201805, `arXiv:hep-ph/0107081 [hep-ph]`.

[61] W. Beenakker, S. Dittmaier, M. Kramer, B. Plumper, M. Spira, et al., *NLO QCD corrections to* $t\bar{t}H$ *production in hadron collisions*, Nucl. Phys. **B653** (2003) 151–203, `arXiv:hep-ph/0211352 [hep-ph]`.

[62] S. Dawson, L. Orr, L. Reina, and D. Wackeroth, *Next-to-leading order QCD corrections to* $pp \rightarrow t\bar{t}h$ *at the CERN Large Hadron Collider*, Phys. Rev. **D67** (2003) 071503, `arXiv:hep-ph/0211438 [hep-ph]`.

[63] S. Dawson, C. Jackson, L. Orr, L. Reina, and D. Wackeroth, *Associated Higgs production with top quarks at the large hadron collider: NLO QCD corrections*, Phys. Rev. **D68** (2003) 034022, `arXiv:hep-ph/0305087 [hep-ph]`.

[64] A. Djouadi, J. Kalinowski, and M. Spira, *HDECAY: A Program for Higgs boson decays in the Standard Model and its supersymmetric extension*, Comput. Phys. Commun. **108** (1998) 56–74, `arXiv:hep-ph/9704448 [hep-ph]`.

[65] A. Bredenstein, A. Denner, S. Dittmaier, and M. Weber, *Precise predictions for the Higgs-boson decay $H \to WW/ZZ \to 4$ leptons*, Phys. Rev. **D74** (2006) 013004, `arXiv:hep-ph/0604011 [hep-ph]`.

[66] S. Actis, G. Passarino, C. Sturm, and S. Uccirati, *NNLO computational techniques: The cases $H \to \gamma\gamma$ and $H \to gg$*, Nucl. Phys. **B811** (2009) 182–273, `arXiv:0809.3667 [hep-ph]`.

[67] LHC Higgs Cross Section Working Group, S. Dittmaier, C. Mariotti, G. Passarino, and R. Tanaka (Eds.), *Handbook of LHC Higgs Cross Sections: 1. Inclusive Observables*, CERN-2011-002 (CERN, Geneva, 2011) , `arXiv:1101.0593 [hep-ph]`.

[68] L. J. Dixon and M. S. Siu, *Resonance continuum interference in the diphoton Higgs signal at the LHC*, Phys. Rev. Lett. **90** (2003) 252001, `arXiv:hep-ph/0302233 [hep-ph]`.

[69] The ATLAS Collaboration, *Updated Luminosity Determination in pp Collisions at $\sqrt{s} = 7$ TeV using the ATLAS Detector*, ATLAS-CONF-2012-080 (2012) .

[70] M. Botje et al., *The PDF4LHC working group interim recommendations*, `arXiv:1101.0538 [hep-ph]`.

[71] H.-L. Lai, M. Guzzi, J. Huston, Z. Li, P. M. Nadolsky, et al., *New parton distributions for collider physics*, Phys. Rev. **D82** (2010) 074024, `arXiv:1007.2241 [hep-ph]`.

[72] A. Martin, W. Stirling, R. Thorne, and G. Watt, *Parton distributions for the LHC*, Eur. Phys. J. **C63** (2009) 189–285, `arXiv:0901.0002 [hep-ph]`.

[73] R. D. Ball, V. Bertone, F. Cerutti, L. Del Debbio, S. Forte, et al., *Impact of heavy quark masses on parton distributions and LHC phenomenology*, Nucl. Phys. **B849** (2011) 296–363, `arXiv:1101.1300 [hep-ph]`.

[74] A. Denner, S. Heinemeyer, I. Puljak, D. Rebuzzi, and M. Spira, *Standard Model Higgs-boson branching ratios with uncertainties*, Eur. Phys. J. **C71** (2011) 1753, `arXiv:1107.5909 [hep-ph]`.

[75] I. W. Stewart and F. J. Tackmann, *Theory uncertainties for Higgs and other searches using jet bins*, Phys. Rev. **D85** (2012) 034011, `arXiv:1107.2117 [hep-ph]`.

[76] J. M. Campbell, R. K. Ellis, and C. Williams, *Hadronic production of a Higgs boson and two jets at next-to-leading order*, Phys. Rev. **D81** (2010) 074023, `arXiv:1001.4495 [hep-ph]`.

[77] Crystal Ball Collaboration, T. Skwarnicki, *A Study of the Radiative Cascade Transitions Between the Υ' and Υ Resonances*, . DESY F31-86-02.

[78] The ATLAS Collaboration and the CMS Collaboration, *Procedure for the LHC Higgs boson search combination in Summer 2011*, ATLAS-PHYS-PUB-2011-011, CMS NOTE-2011/005 (2011) .

[79] A. L. Read, *Presentation of search results: The CL_s technique*, J. Phys. **G28** (2002) 2693–2704.

[80] G. Cowan, K. Cranmer, E. Gross, O. Vitells, *Asymptotic formulae for likelihood-based tests of new physics*, Eur. Phys. J. **C71** (2011) 1554.

[81] E. Gross and O. Vitells, *Trial factors or the look elsewhere effect in high energy physics*, Eur. Phys. J. **C70** (2010) 525–530, `arXiv:1005.1891 [physics.data-an]`.

A Auxiliary plots

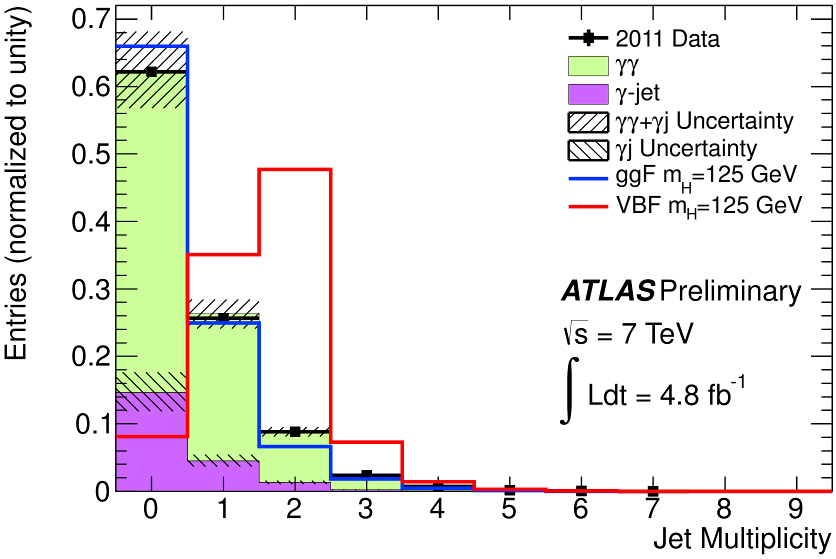

Figure 17: Jet multiplicity in the $\sqrt{s}$ = 7 TeV data compared to simulation. The jets are required to be within $|\eta^{\text{jet}}| < 4.5$ and have $p_{\text{T}}^{\text{jet}} > 25$ GeV. If they are in the tracker acceptance, they are required to have a jet-vertex-fraction of at least 0.75. The $\gamma\gamma$ component is simulated with SHERPA, while the γ-jet component is simulated with ALPGEN, and the small jet-jet and Drell-Yan components are neglected. The two components are normalized such that the final sample has a diphoton purity of 80% as measured on data. The uncertainties on the background components take both the statistical uncertainties of the simulation samples and the uncertainties from the data-driven background decomposition into account. Data and background simulation are found to be in good agreement. The distributions are normalized to unit area to allow for a comparison of the shapes of data and background simulation, and of background and signal simulation. Events from data and background simulation are taken from the mass range between 100 GeV and 160 GeV.

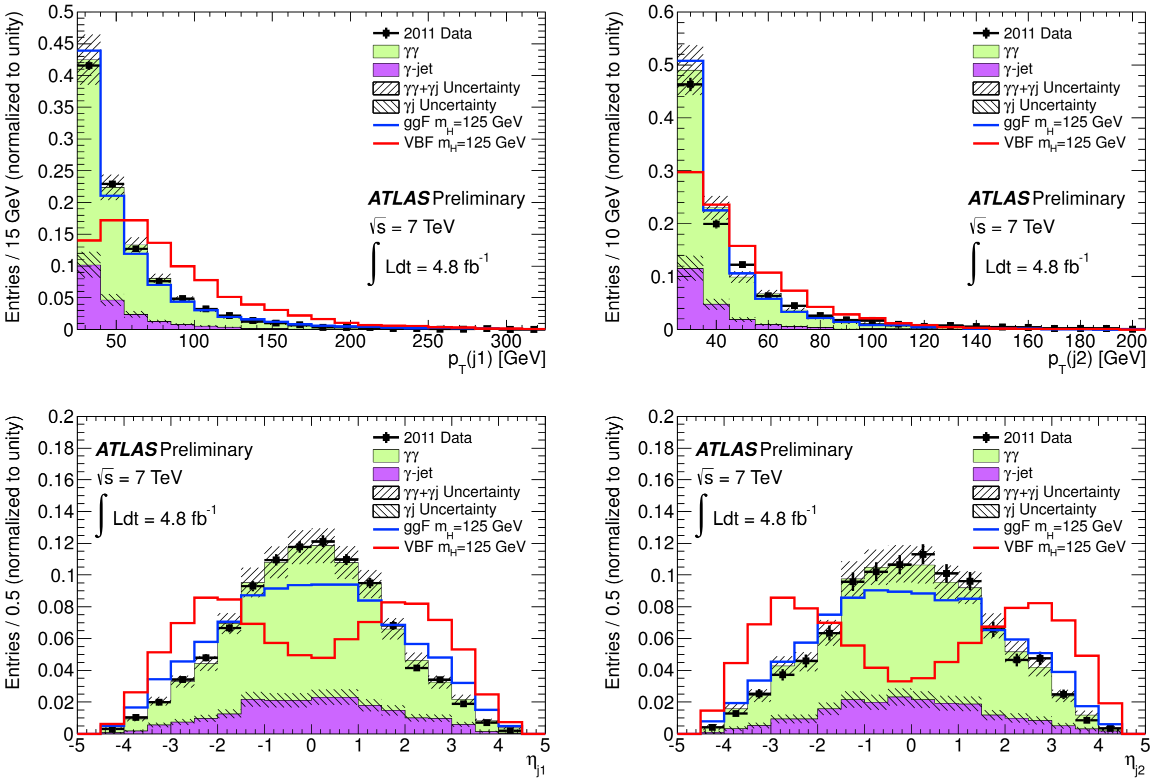

Figure 18: Leading and subleading jet p_{T} (top) and η (bottom) distributions in the $\sqrt{s} = 7$ TeV data compared to simulation for events that have at least two jets fulfilling the following criteria: The jets are required to be within $|\eta^{\mathrm{jet}}| < 4.5$ and have $p_{\mathrm{T}}^{\mathrm{jet}} > 25$ GeV. If they are in the tracker acceptance, they are required to have a jet-vertex-fraction of at least 0.75. The $\gamma\gamma$ component is simulated with SHERPA, while the γ-jet component is simulated with ALPGEN, and the small jet-jet and Drell-Yan components are neglected. The two components are normalized such that the final sample has a diphoton purity of 80% as measured on data. The uncertainties on the background components take both the statistical uncertainties of the simulation samples and the uncertainties from the data-driven background decomposition into account. Data and background simulation are found to be in good agreement. The distributions are normalized to unit area to allow for a comparison of the shapes of data and background simulation, and of background and signal simulation. Events from data and background simulation are taken from the mass range between 100 GeV and 160 GeV.

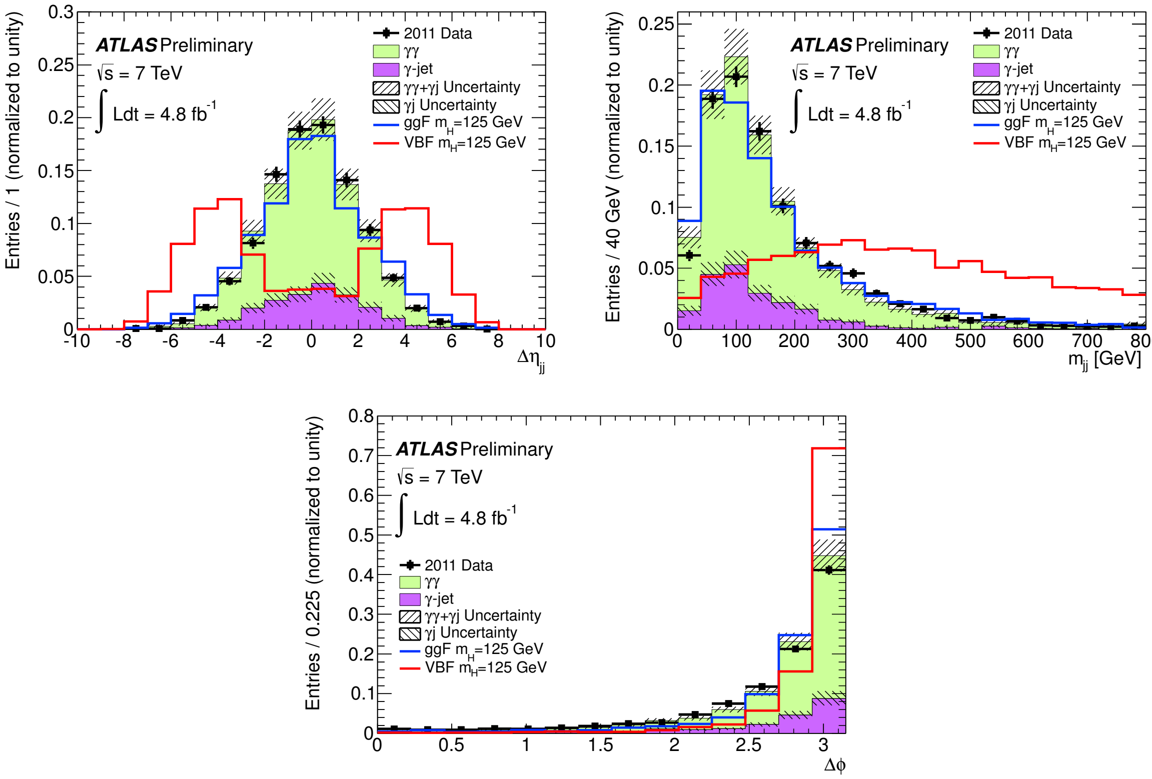

Figure 19: $\Delta\eta_{jj}$, the η separation of the leading and subleading jet (top left), the dijet invariant mass (top right), and the $\Delta\phi_{\gamma\gamma,jj}$, the ϕ separation between the diphoton and the dijet system (bottom plot) in the $\sqrt{s} = 7$ TeV data compared to simulation for events that have at least two jets fulfilling the following criteria: The jets are required to be within $|\eta^{\text{jet}}| < 4.5$ and have $p_{\text{T}}^{\text{jet}} > 25$ GeV. If they are in the tracker acceptance, they are required to have a jet-vertex-fraction of at least 0.75. The $\gamma\gamma$ component is simulated with SHERPA, while the γ-jet component is simulated with ALPGEN, and the small jet-jet and Drell-Yan components are neglected. The two components are normalized such that the final sample has a diphoton purity of 80% as measured on data. The uncertainties on the background components take both the statistical uncertainties of the simulation samples and the uncertainties from the data-driven background decomposition into account. Data and background simulation are found to be in good agreement. The distributions are normalized to unit area to allow for a comparison of the shapes of data and background simulation, and of background and signal simulation. Events from data and background simulation are taken from the mass range between 100 GeV and 160 GeV.

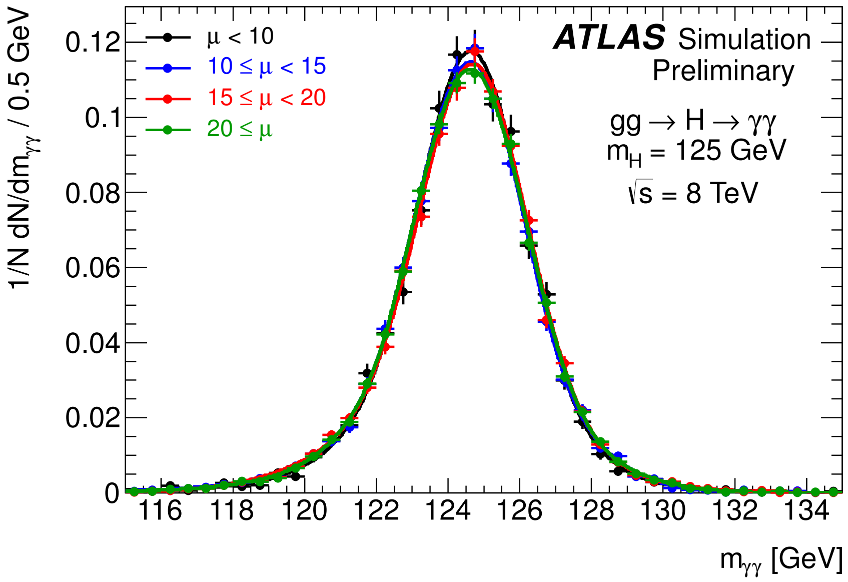

Figure 20: Stability of the invariant mass resolution with pileup.

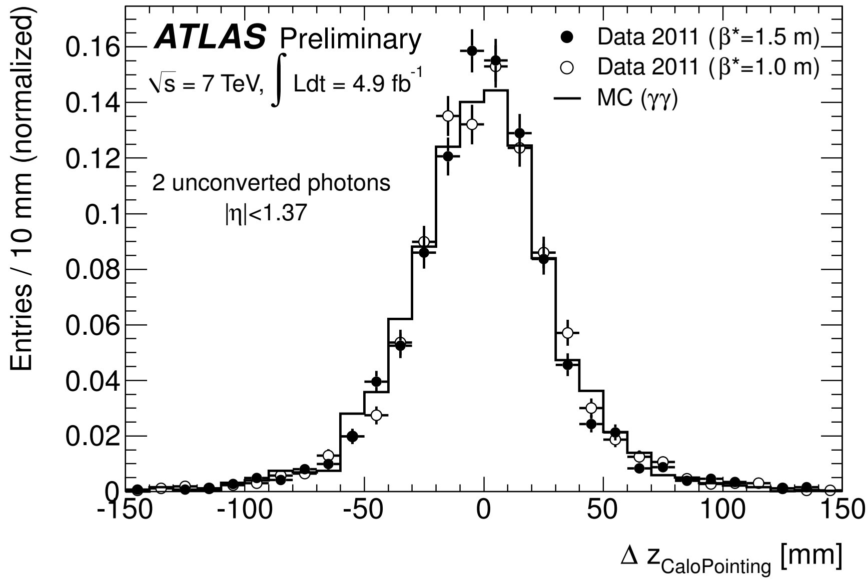

Figure 21: Pile-up impact on calorimeter pointing. This figure shows a comparison between the two estimates of the primary vertex z positions using diphoton events where both photons are unconverted in the barrel region of the electromagnetic calorimeter ($|\eta| < 1.37$). The z position is computed using the calorimeter pointing (energy weighted position of the EM shower in the first and second longitudinal layers of the calorimeter). The data sample is divided into 2 periods with different data taking conditions: the early 2011 data with $\beta^* = 1.5$m ($\langle\mu\rangle \approx 6.3$) corresponding to an integrated luminosity of 2.1 fb^{-1} and late 2011 data with $\beta^* = 1.0$m ($\langle\mu\rangle \approx 11.6$) corresponding to an integrated luminosity of 2.8 fb^{-1}. The resolution observed in data is not sensitive to the different pile-up conditions of the 2 periods. It is in good agreement with the prediction from the Monte Carlo simulation (diphoton MC events).

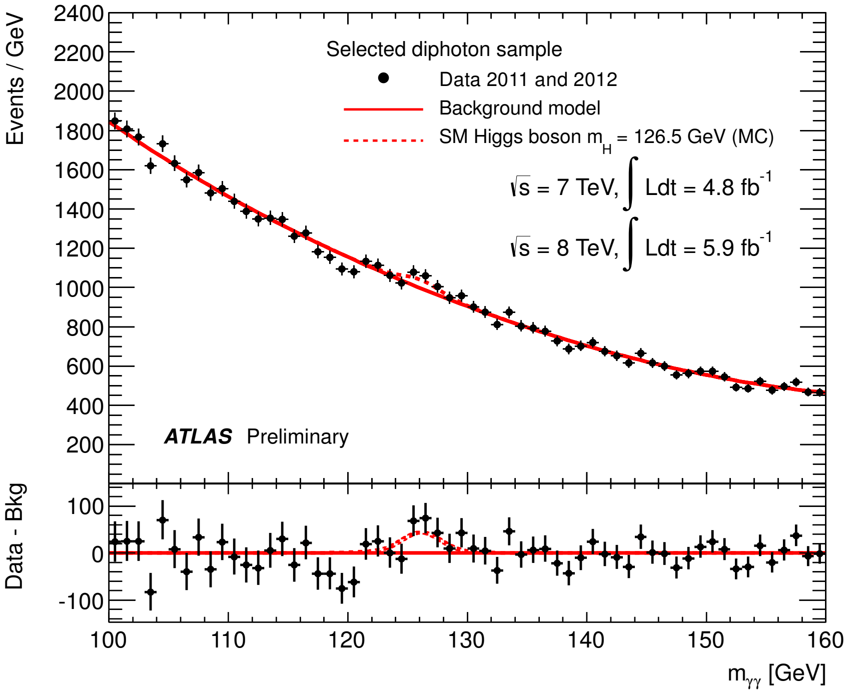

Figure 22: Invariant mass distribution for the combined $\sqrt{s}$ = 7 TeV and $\sqrt{s}$ = 8 TeV data samples, overlaid with the total background obtained from summing the fitted background only models to the distributions in the individual categories. The bottom inset displays the residual of the data with respect to the total background. The Higgs boson expectation for a mass hypothesis of 126.5 GeV corresponding to the SM cross section is also shown.

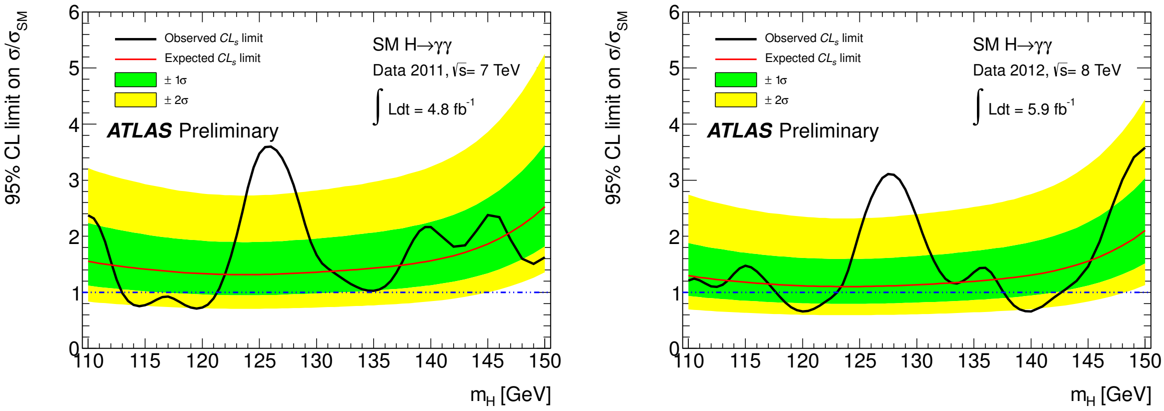

Figure 23: Observed and expected CL_s limit on the normalized signal strength as a function of the assumed Higgs boson mass for the $\sqrt{s}$ = 7 TeV (left) and $\sqrt{s}$ = 8 TeV (right) analyses.

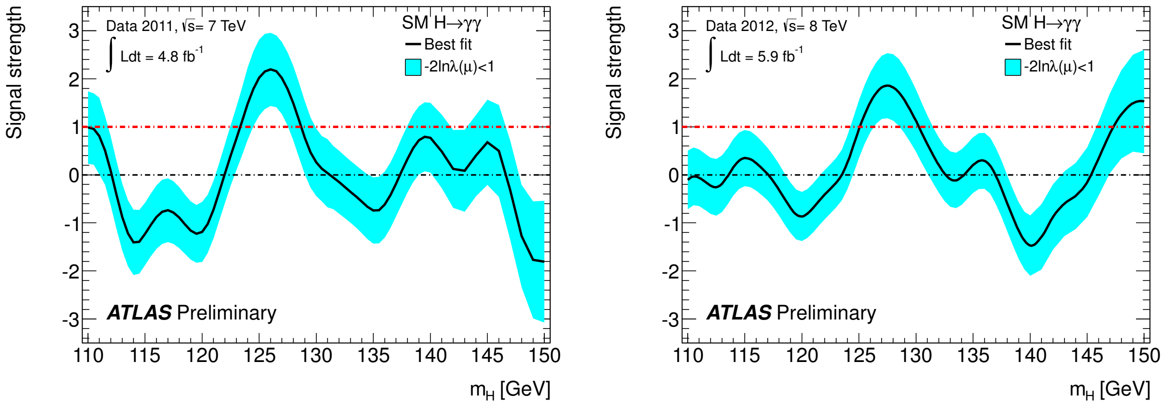

Figure 24: Best fit value for the signal strength as a function of the assumed Higgs boson mass for the $\sqrt{s}$ = 7 TeV (left) and $\sqrt{s}$ = 8 TeV (right) analyses.

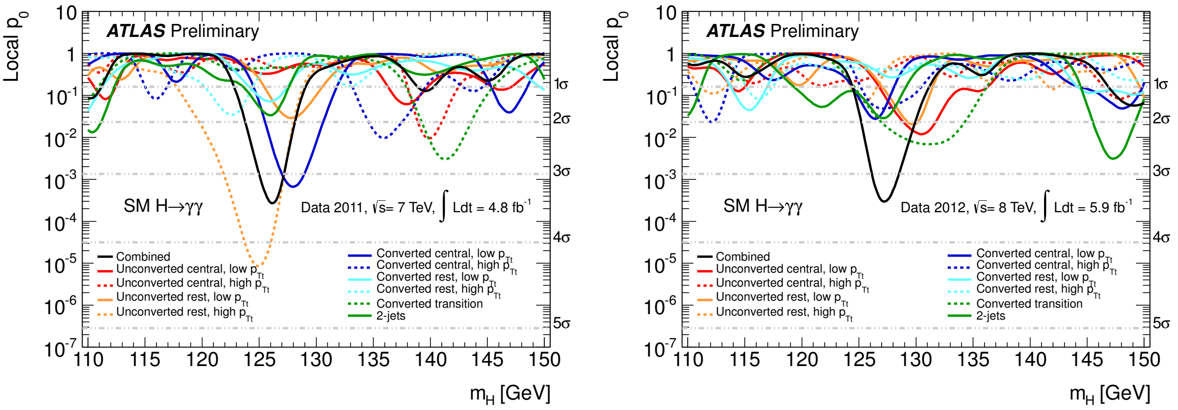

Figure 25: Distributions of p_0 obtained from fits to single categories for the $\sqrt{s}$ = 7 TeV data (left) and the $\sqrt{s}$ = 8 TeV (right), along with the result from the combined fit.

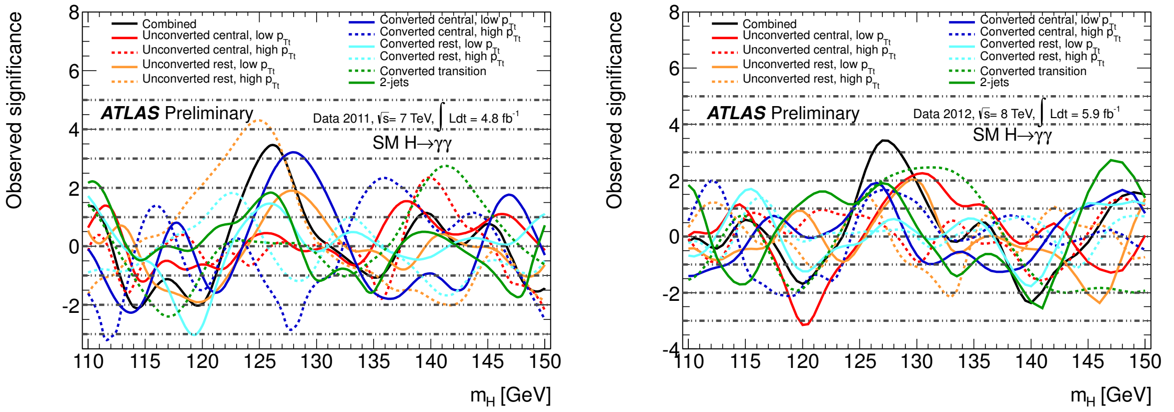

Figure 26: Distributions of observed significance obtained from fits to single categories for the $\sqrt{s}$ = 7 TeV data (left) and the $\sqrt{s}$ = 8 TeV (right), along with the result from the combined fit.

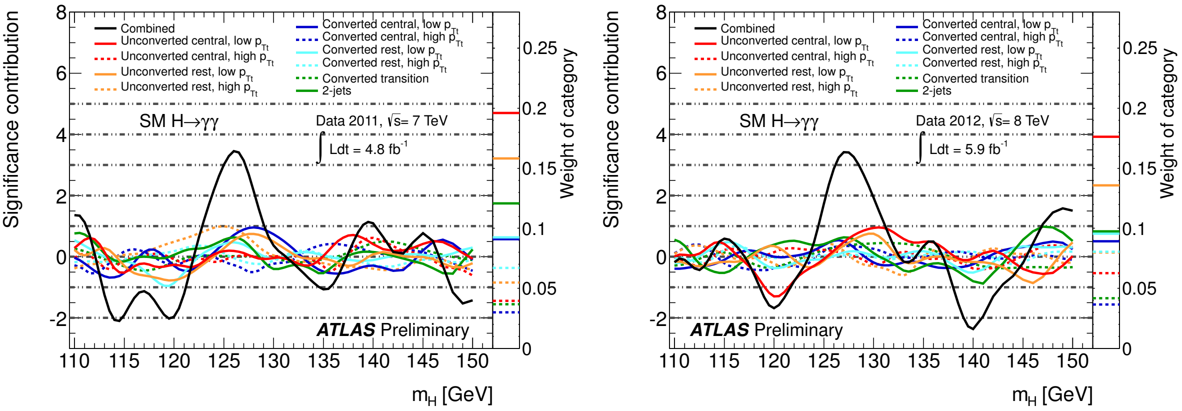

Figure 27: Weighted local significances observed for $\sqrt{s} = 7$ TeV (left) and $\sqrt{s} = 8$ TeV (right) data as a function of m_H. It shows the contribution of the individual categories (colored curves) to the combined result (black). The weights w_i are shown in the right side bar and reflect the expected contribution from each individual category for a SM Higgs boson. They are obtained as $w_i = \frac{\sigma^2}{\sigma_i^2}$, where σ_i and σ are the expected statistical uncertainties on the signal strength per category i and for the combined analysis, respectively. The weighted significances Z_i' are defined as $Z_i' = \sqrt{w_i} Z_i$. The sum of the weighted significances of the categories is approximately equal to the combined significance.

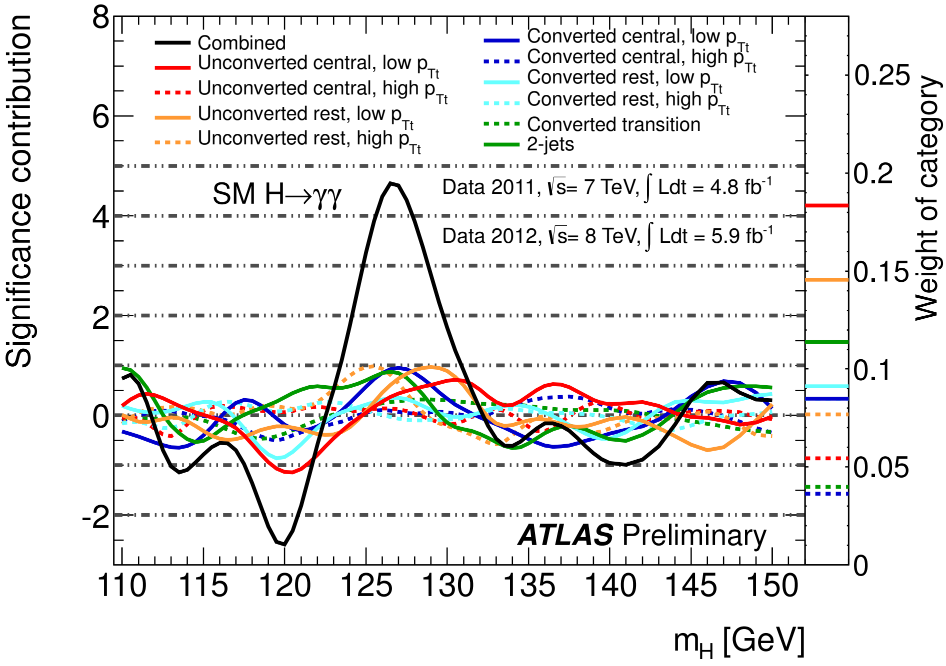

Figure 28: Weighted local significances observed for the combination of $\sqrt{s}$ = 7 TeV and $\sqrt{s}$ = 8 TeV data as a function of m_H. It shows the contribution of the individual categories (colored curves) to the combined result (black). The weights w_i are shown in the right side bar and reflect the expected contribution from each individual category for a SM Higgs boson. They are obtained as $w_i = \frac{\sigma^2}{\sigma_i^2}$, where σ_i and σ are the expected statistical uncertainties on the signal strength per category i and for the combined analysis, respectively. The weighted significances Z_i' are defined as $Z_i' = \sqrt{w_i} Z_i$. The sum of the weighted significances of the categories is approximately equal to the combined significance.

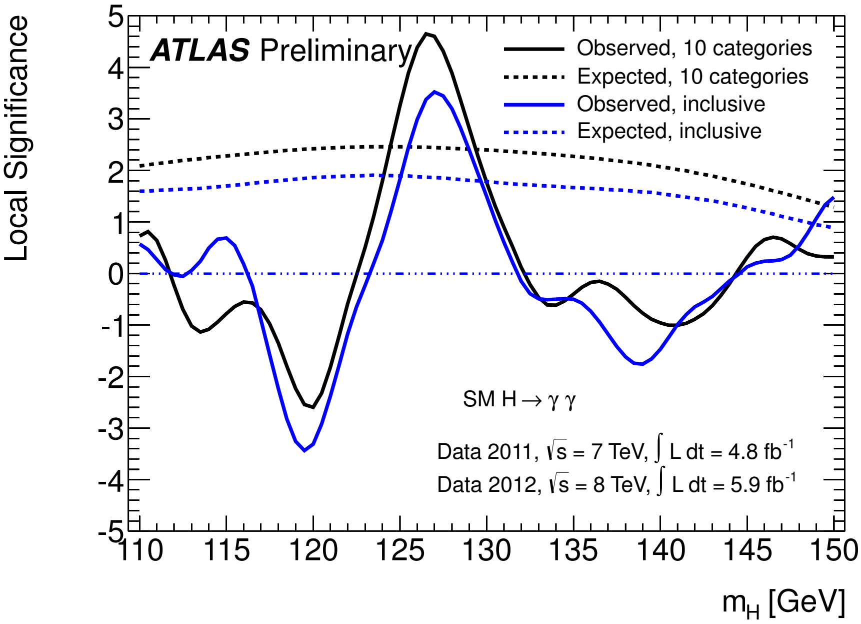

Figure 29: Observed and expected local significance obtained with the analysis using 10 categories, compared with the result of the combined $\sqrt{s}$ = 7 TeV and $\sqrt{s}$ = 8 TeV analysis.

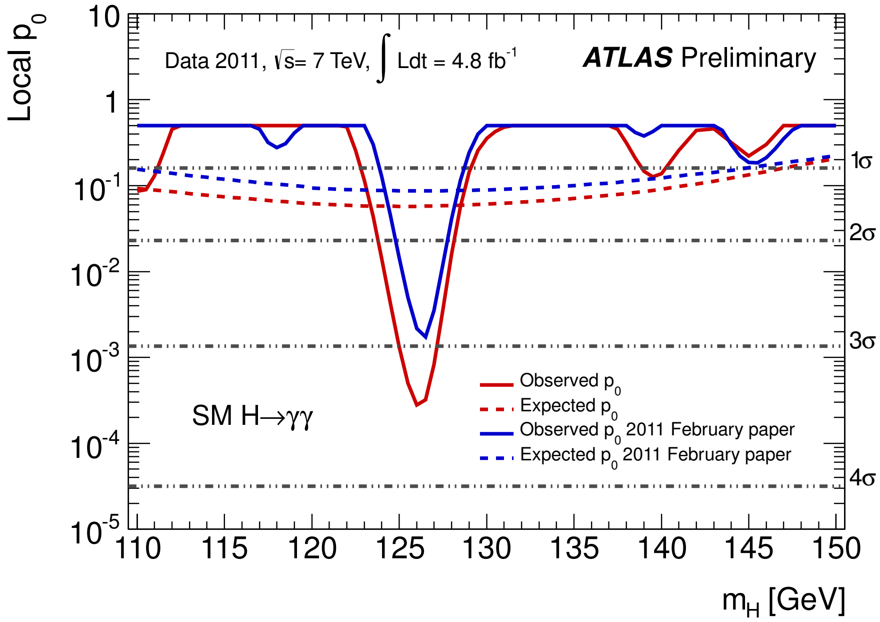

Figure 30: Comparison of the expected and observed capped local p_0 values obtained for the $\sqrt{s}$ = 7 TeV data sample with the analysis published in [8] and the new analysis presented here. The capped p_0 is shown for consistency with the prescription used in [8].

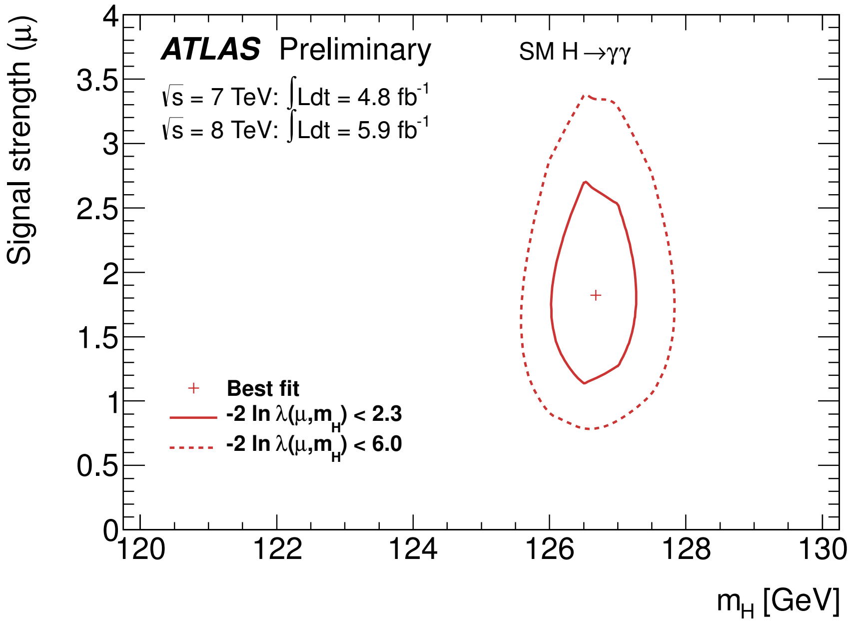

Figure 31: Likelihood contours in the (μ, m_H) plane. The photon energy scale systematic uncertainty has not been considered. The contours are for the combined $\sqrt{s}$ = 7 TeV and $\sqrt{s}$ = 8 TeV analysis and correspond to 68% and 95% CL contours.

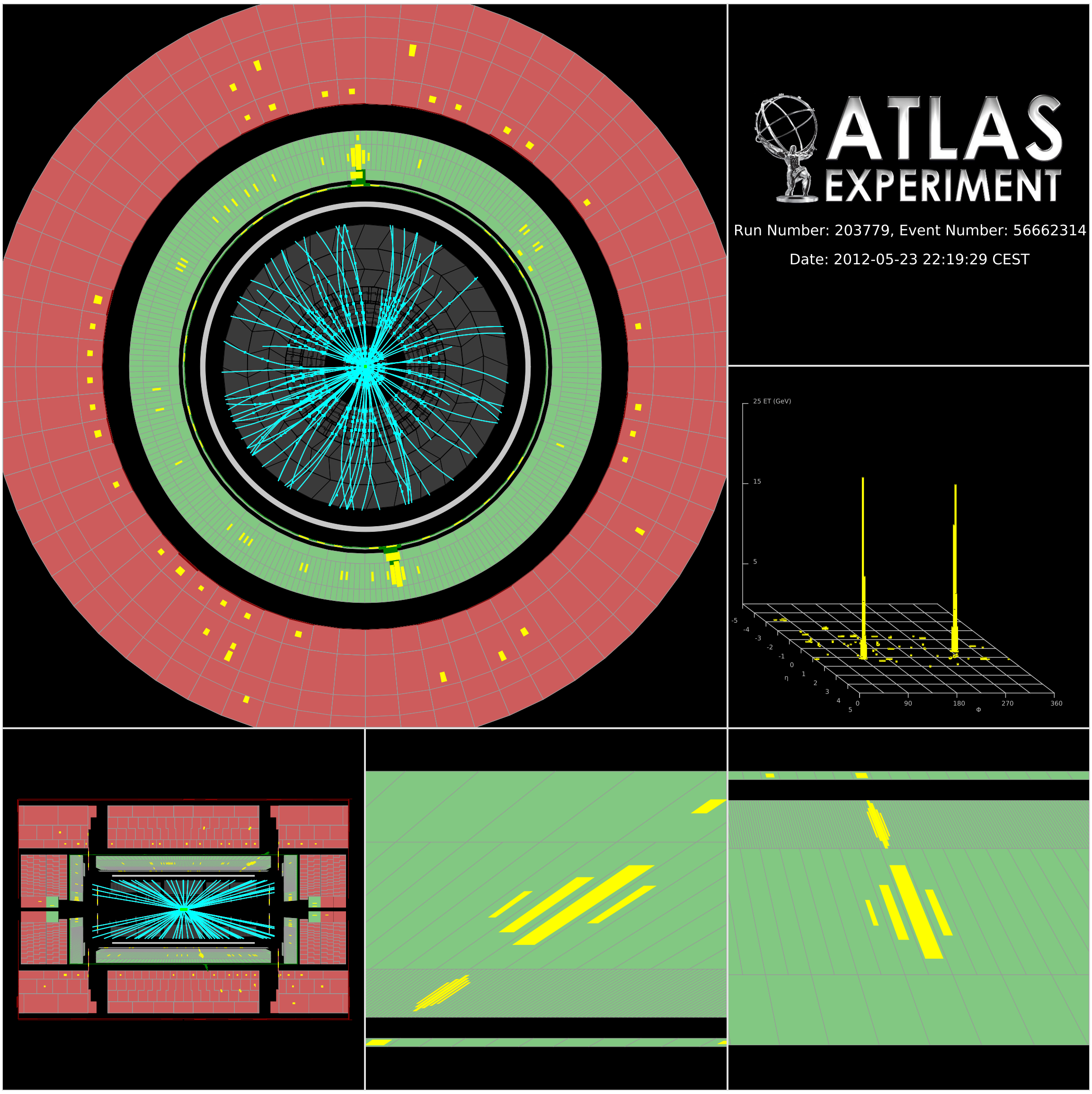

Figure 32: Event display of a diphoton event candidate where both photon candidates are unconverted. The event number is 56662314 and it was recorded during run 203779 at $\sqrt{s}$ = 8 TeV. The leading photon has E_{T}=62.2 GeV and η =0.39. The subleading photon has E_{T}=55.5 GeV and η =1.18. The measured diphoton mass is 126.9 GeV. The p_{T} and $p_{\mathrm{T}t}$ of the diphoton are 9.3 GeV and 6.5 GeV, respectively. Only reconstructed tracks with p_{T}>1 GeV, hits in the pixel and SCT layers and TRT hits with a high threshold are shown.

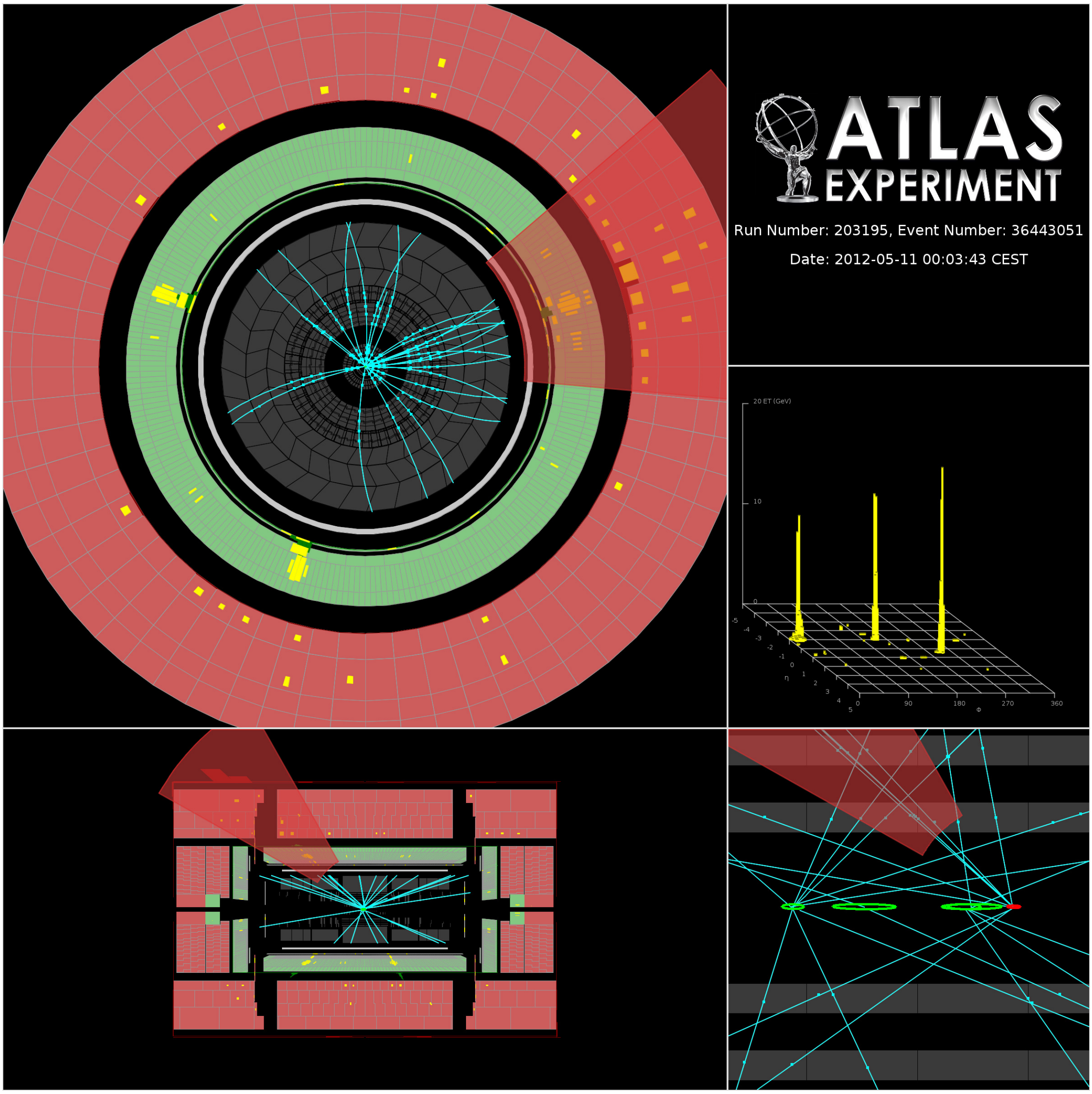

Figure 33: Event display of a diphoton with a jet event candidate where both photon candidates are unconverted. The event number is 36443051 and it was recorded during run 203195 at $\sqrt{s}$ = 8 TeV. The leading photon has E_{T}=63.0 GeV and η =0.50. The subleading photon has E_{T}=56.1 GeV and $\eta = -0.96$. The measured diphoton mass is 127.0 GeV. The p_{T} and p_{Tt} of the diphoton are 83.9 GeV and 83.3 GeV, respectively. The jet has E_{T}=113 GeV and $\eta = -0.9$. Only reconstructed tracks with p_{T}>1 GeV, hits in the pixel and SCT layers and TRT hits with a high threshold are shown.

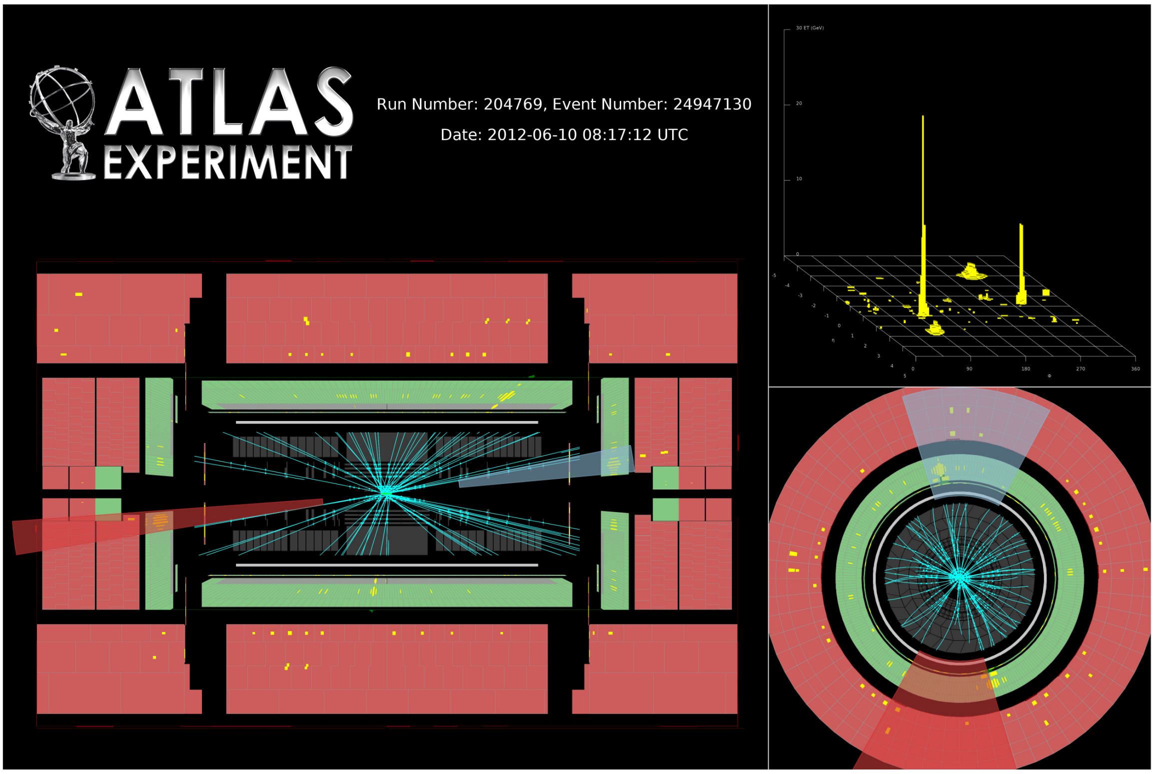

Figure 34: Event display of a diphoton with two jets event candidate where both photon candidates are converted. The event number is 24947130 and it was recorded during run 204769 at $\sqrt{s}$ = 8 TeV. The leading photon has E_{T}=80.1 GeV and η =1.01. The subleading photon has E_{T}=36.2 GeV and $\eta = -0.17$. The measured diphoton mass is 126.9 GeV. The p_{T} and p_{Tt} of the diphoton are 44.3 GeV and 6.2 GeV, respectively. The leading jet has E_{T}=120 GeV and $\eta = -2.9$. The subleading jet has E_{T}=81 GeV and η =2.7. The measured two-jets mass is 1.6 TeV. The $\Delta\phi$ between the diphoton system and the system of the two-jets is 2.9. Only reconstructed tracks with p_{T}>1 GeV, hits in the pixel and SCT layers and TRT hits with a high threshold are shown.